The Pennsylvania State University

The Graduate School

Department of Geosciences

PASSIVE ACOUSTIC MONITORING OF COARSE BEDLOAD IN MOUNTAIN STREAMS

A Thesis in

Geosciences

by

Jonathan Shailer Barton

Submitted in Partial Fulfillment
of the Requirements
for the Degree of

Doctor of Philosophy

August 2006

The thesis of Jonathan Shailer Barton was reviewed and approved* by the following:

Rudy L. Slingerland
Professor of Geology
Thesis Advisor
Chair of Committee

Richard B. Alley
Professor of Geosciences

Charles J. Ammon
Associate Professor of Geosciences

Thomas A. Gabrielson
Professor of Acoustics

Peggy A. Johnson
Professor of Civil Engineering
Special Signatory

Timothy J. Bralower
Professor of Geosciences
Department Head

*Signatures are on file in the Graduate School

ABSTRACT

A method for monitoring bedload transport rate using commercial hydrophones is presented. The results of flume experiments comparing acoustic power to video of bedload transport confirm earlier work showing a linear relationship between acoustic power and bedload transport rate. These results also show that acoustic methods have the potential to record changes in transport rate at high temporal resolution. Field experiments, conducted during the May 2005 Trinity River (California) dam release, show that a linear prediction of bedload transport compares well with pressure-difference sampler data, and suggests that acoustic data can be used to fill data-gaps between sampling periods. The field data also suggest that a single calibration relationship can be applied over a month-long snowmelt-type flood event. A computer model of acoustic production is presented, and is used to confirm the linear relationship between transport rate and acoustic power observed in the flume and in previous work. The model also shows that a single hydrophone may be highly sensitive to changes in the cross-stream distribution of bedload transport.

TABLE OF CONTENTS

LIST OF FIGURES

LIST OF TABLES

ACKNOWLEDGEMENTS

This work was partly funded by grant EAR 01-26131 awarded to Rudy L. Slingerland, Thomas B. Gabrielson, and Niels Hovius, by the National Science Foundation. I would like to thank Rudy Slingerland, my advisor, for much support over the years. Tom Gabrielson provided patient and frequent electronics and acoustics support: both in time and in components. Chuck Ammon gave generously of his time for discussions, and of his knowledge of normal modes. Peggy Johnson graciously allowed me and a ton of gravel to take over her flume for six months. I would like to thank John R. Gray, U.S.G.S., for his undying enthusiasm, and for his efforts, finally successful, in finding a field site where we could test this technology. I'd like to thank Andreas Krause, of the Trinity River Restoration Project, for looking out for my safety on the river. Graham Matthews and Associates, and especially Graham Matthews, Smokey Pittman, Wes Smith, and Cort Pryor provided logistical help in the field, and answered endless questions during data processing. I would also like to thank Liz Keppler of the U.S.F.S. Redwood Sciences Laboratory in Fort Bragg, California for her assistance at Caspar Creek. Scott Miller, Doug Edmonds, Ellen Hermann, and many others at Penn State provided stimulating conversations that certainly contributed to this work. I thank my parents and my sister for getting me to this point, and especially, I would thank my wife, Jennifer Walters, for putting up for so long with a husband in graduate school.

Chapter 1

Introduction

There has long been a need to monitor bedload fluxes in mountain streams, but few practical methods for observation. There is a particular need to measure the coarser fraction of the bedload in mountain streams because it is this fraction that reduces reservoir capacity. In addition to the obvious engineering needs, recent attempts to better understand bedrock erosion in steep mountain streams [e.g. *Hartshorn, et al.*, 2002] have underscored the need for a better method to measure bedload accurately, especially during high-flow events. The prevailing view of fluvial bedrock erosion [e.g. *Slingerland, et al.*, 1997; *Howard*, 1998; *Sklar and Dietrich*, 1998; 2004] considers both hydraulic plucking and abrasion by bedload particles to be responsible. Therefore, in order to make predictions about downcutting in these channels, it is necessary to have accurate measurements of the rate of availability of abrasion tools.

Bedload flux in coarse-bedded and bedrock channels is difficult to predict primarily because it is poorly correlated with water discharge. Traditional prediction methods that rely on the concept of transport capacity are therefore inapplicable to these streams. In coarse-bedded streams, the bed is typically armored, and interlocking of the armor grains makes prediction of armor failure impossible using traditional models of shear stress and grain size. In bedrock streams, there is typically less sediment available for transport than the capacity-driven models would predict. Where there is sediment available, it may also be armored, further complicating the prediction process.

The inadequacies of bedload flux predictions drive the need for observation-based descriptions of transport phenomena. Bedload flux is highly variable in both space and time, which requires the observer to take measurements closely spaced in both of these variables, to fully characterize the phenomena.

Coarse-bedded streams have posed unique difficulties for field observers as well. Pressure-difference samplers [*Helley and Smith*, 1971; *Emmett*, 1980] are the most commonly used sampling device. These are typically suspended either from a cableway/bridge or from a boat. The rough bed can make it difficult to set a sampler wholly within the bedload transport zone. High flow rates common in these steep streams make sampling with a suspended instrument difficult because of instability, and because at high flow rates, disruption of the hydraulics around the sampler is exaggerated. There is also increased risk of sampler damage from high-velocity particles striking the instrument. At high flow-rates there is also increased safety risk for sampler operators, which must be offset by increased costs.

Vortex samplers [*Klingeman, et al.*, 1979] provide the most complete record of transport, as they cover the full width of the river and sample continuously. However, those built in the past have been extremely expensive to build and to operate. Slot samplers such as the Birkbeck sampler [*Reid, et al.*, 1980; *Lewis*, 1991] have been used to obtain continuous observations, but these are expensive to install, and typically require human intervention during operation. For example, Lewis [*Lewis*, 1991] reports on the hazards associated with emptying the pits of a modified Birkbeck sampler during a high-flow event. To obtain 100% sampling efficiency with either the vortex or the slot

samplers, they must be 100-200 times the width of the largest particle moving. In a cobble or boulder reach, this is prohibitively large.

During high-discharge flows, however, none of the available methods is effective, and all have difficulty measuring the spatial and temporal variability of the transport rate. One can monitor check dams through time to calculate long-term fluxes, but this method is labor intensive, and does not provide real-time estimates. Generalizing these data to other unmonitored catchments is problematic because the transport rate of the coarse fraction increases as a higher power of the fluid shear stress. Thus, a few infrequent events may be responsible for the bulk of the transport.

Acoustic methods present an opportunity for measuring bedload flux during both high and low flows. Although many attempts have been made to use these methods to measure fluvial bedload [e.g. *Mühlhofer*, as cited in *Bedeus and Ivicsics*, 1964; *Bedeus and Ivicsics*, 1964; *Johnson and Muir*, 1969; *Bänziger and Burch*, 1990; *Govi, et al.*, 1993], recent advances in technology have rendered these methods accessible. Most acoustic methods do not appreciably change the hydraulic conditions near the bed. These methods provide continuous data, and because acoustic signals travel great distances in water, they integrate over a large area of the bed.

Three main hypotheses will be tested in this work: 1) Bedload transport rate can be inferred from the acoustic power produced by collisions occurring during transport. 2) The relationship between the acoustic power generated by sediment collisions and bedload transport is linear in form, as has been put forward by past researchers (e.g. Johnson and Muir [1969], Jonys [1976]). 3) This relationship can be exploited to produce

a viable instrument system for the measurement by proxy of bedload transport in the field.

In order to test these hypotheses, several methods were employed. These methods will be described in the following sequence. First, the state of community knowledge is presented. Chapter 3 outlines the theoretical basis for two mechanisms for the production of sound during the collision of sediment grains. Chapter 4 contains a description of the electronics used in the subsequent experiments. In Chapter 5, the design of, and results from, a computer model simulating spatially distributed sediment collisions are presented. Chapter 6 contains the description of two experiments, conducted in a recirculating flume, examining the relationship between observed bedload transport rate and acoustic power. Chapter 7 contains the description of a field experiment conducted in May 2005 at the Trinity River, California, which has been submitted for publication [*Barton, et al.*, submitted]. The authors of the paper were: Jonathan S. Barton, Rudy L. Slingerland, Smokey Pittman, and Thomas B. Gabrielson. Jonathan S. Barton (this author) conceived of the project goals, collected the acoustic data, and wrote most of the paper. Rudy L. Slingerland and Thomas B. Gabrielson contributed with discussions, editorial comments, and technical expertise. Smokey Pittman contributed a technical description of the pressure-difference data collection, a version of which is included in this work.

Chapter 2

Background

> In the past, attempts have been made to determine the bedload discharge in three general ways: By direct measurement with some type of apparatus; by definition of physical relations from which the bedload could be estimated; and by quantitative measurements of the results of some sedimentation process, such as erosion or deposition. Unfortunately, direct-measuring apparatus have been useful for only a very limited range of sediment and hydraulic conditions; the definition of physical relations has not been complete enough to estimate the bedload discharge; and the quantitative measurements have supplied information only on the characteristics of the reach that was studied. As a result, no single apparatus or procedure, whether theoretical or empirical, has been universally accepted as completely adequate for the determination of bedload discharge over the wide range of sediment and hydraulic conditions in nature. [*Hubbell*, 1964]

Bedload Flux Measurements

Basket samplers were the first bedload monitoring devices that were put into use. In the early 1930s, Ehrenberger [*Ehrenberger*, as cited in *Hubbell*, 1964] tested several basket samplers in Austria, and first made efficiency measurements of the designs. Ehrenberger attributed the original sampler design to Mühlhofer, but Ehrenberger and others added a flexible chain-link bottom to conform to the bed shape, and made other improvements to generally increase the sampling efficiency. These samplers were used both for the solution of specific fluvial problems, as well as to test bedload transport equations. [*Hubbell*, 1964]

The next major type of bedload sampler to emerge was the pressure-difference sampler, which though first made by Goncharov in 1929 [described in *Hubbell*, 1964], became widely used with the advent of the Arnhem sampler in the 1940s. Pressure-difference samplers employ the decrease in water pressure downstream of an expanding nozzle to offset the pressure buildup created by the mesh capture bag. Helley and Smith [1971], while using the same expansion ratio as the Arnhem (3.22), changed the nozzle shape from a 8 ×16 cm opening to a 3 × 3 in opening to create the Helly-Smith sampler, which has seen much use in the past three decades in its original size and in a double-scale 6 × 6 in nozzle opening. In 1985, the U.S. Geological Survey Water Resources Division gave the name of BL-84 to a modified Helley-Smith sampler with a 3 × 3 in nozzle and a 1.40 expansion ratio, which was shown to have a more consistent sampling efficiency over a range of grain sizes than the earlier models [*Hubbell, et al.*, 1985]. Subsequent work by Childers [1999] introduced the Toutle River-2 (TR-2) sampler, which has the same 1.4 expansion ratio as the BL-84, but has a 6 × 12 in opening. It also uses a bilateral tail-fin system, which moves the tail out from the turbulent wake produced by the sample bag; this arrangement increases the stability of the TR-2 in high flow environments. At present, the BL-84 sampler is the only sampling device currently approved by the U.S. Geological Survey for use. All of these samplers are limited in the particle size for which they will be effective. Childers [1999] admonishes about the use of the Helley-Smith/BL-84 3 × 3 in nozzle when intermediate grain diameters exceed 16 mm, the 6 × 6 in nozzle when intermediate grain diameters exceed 32 mm, and the 6 × 12 in nozzle when intermediate grain diameters exceed 64 mm.

In an effort to better average out temporal variability inherent in bedload transport, researchers turned to slot or pit samplers, led in 1940 by Mülhofer [described in *Hubbell*, 1964]. His work was followed by Einstein [*Einstein*, 1944], who established the size limitations for slot samplers, assumed a logarithmic probability distribution for saltation lengths, which led him to suggest that a slot that is approximately 600% longer than the mean saltation length of a given particle size will result in 99.8% trapping efficiency for that size. These efforts were followed by the much more ambitious vortex sampler at Oak Creek, Oregon, reported by Klingeman et al. [*Klingeman, et al.*, 1979]. This system induces a fluid vortex in a transverse slot in the riverbed, which continuously removes sediment from the channel to be weighed. This allowed the examination of the temporal variability of transport, although because of delays, the time-resolution was not very high. The less expensive Birkbeck pit sampler was developed by Reid [*Reid, et al.*, 1980], which used pressure pillows to continuously weigh sediment accumulating in bins placed in pits. Lewis [*Lewis*, 1991] modified the sampler to use a piezoelectric load cell rather than a pressure pillow, which reduced temperature dependence and frequency of malfunction. Both forms of the Birkbeck sampler have the disadvantage that the bins must be emptied, sometimes at the height of flood, which is a labor-intensive, dangerous task.

Many other types of samplers have also been tested, such as tray or pan samplers, but few of them have survived into contemporary use. Hubbell [*Hubbell*, 1964] gives an exhaustive review for the early part of the twentieth century. Recently, new developments in the use of active acoustics, in particular, the bottom-tracking capability of acoustic doppler current profilers, in combination with GPS to estimate the rate of movement of

the bed shows some promise for bedload measurement, especially in smaller grain sizes. [*Rennie, et al.*, 2002]

Passive Acoustic Monitoring

Monitoring bedload transport using acoustic methods is not a new idea. Instruments designed to record the sound from sediment can be divided easily into two different types. The first type records the sound generated when sediment grains collide with a part of the sensor apparatus (instrument-induced noise), which could be a plate, rod, or pipe. The second type records the sound generated when sediment grains collide with each other, or with bedrock (self-generated noise).

Instrument-Induced Noise Detection

Recording the noise caused by the collision of moving bedload with a metal plate originated in 1933 with Mühlhofer [*Mühlhofer*, as cited in *Bedeus and Ivicsics*, 1964], on the Inn River, in Austria. A watertight steel box, which housed a microphone, was placed on the bed of the river. Bedload particles collided with the upstream-facing plate of the box, which produced acoustic energy within the box. The microphone signal was then conveyed through an amplifier to headphones, with which Mühlhofer attempted to manually count the number of impacts.

The Grenoble Laboratory [*Labaye*, 1948] placed a triangular steel plate on the bed of the river, with a microphone in a watertight box above, and the noise of sediment

moving over the plate was transmitted to the microphone through a steel bar that was connected to both the plate and the microphone membrane. No results were reported from the use of this instrument, however.

Braudeau [1951], modifying the Grenoble instrument, moved the microphone into direct contact with the plate, which he also changed to brass. The resulting sound was amplified and transmitted to headphones. There was no attempt made to record the sound, although it was suggested as a future step. The instrument was tested during two releases from the Viclaire hydroelectric facility, and Braudeau qualitatively described the bedload transport. He was able to determine a motion-inducing discharge to within 1 m^3/s, but did not attempt to quantify the bedload transport rate.

Juniet [1952], who was concerned that previously developed methods were not suitable for fine-bedded rivers, created a tripod, which supported a 20 cm forked rod inserted vertically into the bed of the river. Moving sediment struck the rod and induced vibrations, which were transmitted to a piezoelectric transducer. Magnetic tape recordings of sand collisions were produced.

Hinrich [*Hinrich*, 1970] modified the Grenoble Laboratory sensor to use a hydrophone instead of the microphone assembly used previously. He also replaced the steel plate with brass. The hydrophone signal was amplified and transmitted to headphones. He was able to detect a critical discharge for bedload movement using the device, but was unable to calculate transport rates. He also installed a hydrophone on an Arnhem sampler, and used it to "verify" the sampler data. He stated that variations in the bedload transport as it entered the sampler were "easily heard". For both of these installations, no quantitative results were reported.

Bänziger and Burch [1990] and later Rickenmann and others [*Rickenmann et al.*, as cited in *Bogen and Møen*, 2001] described a system that uses a piezoelectric crystal transducer to record impacts of sediment on a metal plate mounted on the riverbed. Bänziger and Burch also used an impulse counter when impact amplitude exceeded a threshold. The paper reported results from four years of data collection on a mountain stream in Switzerland. Bänziger and Burch also presented a plot of discharge and impulse rate that clearly showed a clockwise hysteresis between impulse rate and discharge. However, they did not present any comparison with traditional bedload measurement techniques.

Bogen and Møen [2001] described a similar system, where an unidentified transducer (I speculate that it was an accelerometer) was mounted on the underside of a steel plate mounted on the bed of the river. This system had the advantage that it did not protrude into the flow, though it required access to the bed of the stream at low water for installation. They restricted their analysis to the vibration in a narrow, ultrasonic frequency band, but unlike Bänziger and Burch who counted impacts, they used acoustic amplitude as their proxy for bedload transport. The steel plate measured 0.5 × 0.5 m, and was 10 mm thick. They presented comparisons between water discharge and acoustic amplitude, which showed good agreement. They also performed a comparison with eight Helley-Smith samples, which showed a general trend of increasing acoustic amplitude with increasing sample size; however, no statistical analysis was reported.

Carling and others [*Carling, et al.*, 2001] also affixed an accelerometer and data logger to the bottom of a steel plate, which was then anchored to bedrock in Birk Beck. They counted the number of impacts on the plate and attempted to relate that to bedload

transport. They noted that the instrument could not count impacts occurring closer together than once every third of a second, and showed an example of saturation in the data that resulted from this limitation. Their impact plate measured 15 × 13 cm in area, and 6 mm in thickness. Thus, it also delivered a localized view of the sediment transport. They used the system to detect onset of bedload movement, as well as lateral variability of transport. They argued that the minimum detectable particle size was 55-70 mm, and that the critical shear stress for onset of motion varied between 40-100 Pa, and cessation of transport occurred at 40-50 Pa. One of the chief advantages of this type of sensor, which the authors pointed out, is its durability in the presence of high flows and large moving particles. They reported that it survived, and operated throughout, a flood in which particles as large as 1 m were moving. Also, the unit was self-contained and was capable of unattended operation for six months.

Downing and others [*Downing, et al.*, 2001; *Downing and Ryan*, 2001] tested a pressure-plate gravel-transport sensor. The sensor consisted of a steel pressure-plate backed by an aluminum support. Gravel colliding with the pressure-plate compressed piezoelectric film, which generated an electric charge proportional to the force exerted on the pressure-plate. The system was designed to be installed on the streambed, or to be deployed by a wading operator. In either configuration the sensor, which had a triangular cross-section when viewed from above, was placed with the pressure plate at a 45° angle to the flow and perpendicular to the bed. This configuration produced a minimum in the variability in output caused by slight variations in the impact angle of the bedload particles. The handheld version of the instrument was slightly smaller than the mounted version, but was otherwise similar. The anchored version was mounted on an anchor

assembly, which housed batteries, a data logger, and a pressure transducer to record water depth. The electronics used a threshold charge to detect impacts, and recorded the length of the pulse, as well as the integral of the charge over the pulse duration. This integral was proportional to the momentum of the colliding particle. Making assumptions about the velocity of the particles colliding with the sensor, the authors then converted the results into mass transport rates. The data presented showed general agreement with data from bedload traps installed on the bed, with some notable exceptions. The authors attributed these differences to uncertainties in particle velocities and lateral variability in sediment transport rate, because the test sensors were placed adjacent to the traps on the bed.

Froehlich [2001] reported on a system consisting of three 6 m steel pipes placed horizontally on the bed of the Bacza stream, in the Homerka catchment of the Polish Flysch Carpathians.. (No further orientation information is given by Froehlich.) The pipes were spaced 10 m apart, and each housed a small capacitive microphone. He detected noise generated by sediment collisions within a relatively narrow frequency band (20-60 Hz). The acoustic data were processed by a low-frequency amplifier, and six filters, and passed to a data logger, which recorded the amplitude of the current produced by the amplifier.

Mizuyama et alii [*Mizuyama, et al.*, 2001] placed a hydrophone within a steel pipe in the slot of a sediment control dam on the Joganji River. They counted the number of acoustic pulses produced as sediment moved through the dam, and impacted the pipe. The preliminary data that were given showed a good agreement between the hydrograph and the acoustic pulse count, with the pulse count shifted earlier in time.

Self-Generated Noise Detection

The first to attempt to record the self-generated noise of sediment transport in rivers were Bedeus and Ivicsics [1964], who used a directional crystal microphone encased in a boat-mounted, streamlined steel housing to record bed motion on the Danube. The microphone was connected to an analog integrator to dampen high-frequency changes in the current signal. The output of the instrument was connected to headphones and to an ammeter, with an analog display, which was observed by the operator and values were recorded manually. Bedeus and Ivicsics found that the output of the microphone system was not dependent on the deployment height above the bed, and as a result deployed the instrument within 1 m of the river surface, to minimize deflection of the suspension cable. Deflection was a problem, because the microphone was directional, and its aim was determined by the cable direction. The authors suggested a method to overcome this dependence, but did not apply it, as they were able to work within the top meter of the water column. The instrument was used to examine lateral variability in bedload transport and the results were compared to sampler data from the same cross-section. There is a dramatic difference between the two results, which the authors attribute to inaccuracy and unreliability of the sampling methods used. Bedeus and Ivicsics also used the instrument to compare bedload transport patterns at different cross-sections, and showed that cross-stream patterns of high noise content are not consistent over distances of 10 km.

Johnson and Muir [1969] reported on flume experiments with a piezoelectric microphone, and also derived a theoretical relationship between transport rate and

microphone output based on a saltation length formula from Einstein, the Hertz Law of Contact, and the Meyer-Peter and Müller gravel transport equation. Using their flume data, Johnson and Muir empirically determined the constants in their theoretical formulation, which depend on the electrical characteristics of the recording system, along with the material properties of the sediment and water. They also showed that their theoretical formulation does not significantly improve on a power-law fit to the data. They point out that some degree of scatter in the data is expected because the two devices involved (the microphone, and a continuously-weighing pit sampler) are measuring different phenomena. The acoustic results provide a measure of the amount of moving sediment over a spatial area, whereas the pit sampler provides a measure of the amount of sediment passing through a cross-section. While these two phenomena could be expected to correlate, they should not be expected to have unity correlation.

Tywoniuk and Warnock [1973] used a hydrophone encased in a steel fish on the Vedder River in British Coloumbia. Using analog filters, they subdivided the signals into nine frequency bands, but compared all of the data against rating-curve derived bulk bedload transport rates. They were unable to develop a quantitative relationship based on the small amount of data that they processed. Their hydrophone system, like that of Bedeus and Ivicsics, was suspended in the high-velocity flow, which generated much turbulent noise that obscured the bedload signal, and may, to some extent, have produced a spurious correlation with the rating-curve estimate of bedload transport.

Anderson [1976] simplified the system of Johnson and Muir [1969] to study the variation in bedload transport in a small, sand-bedded stream near Bristol, UK. No contemporaneous measurement of bedload transport was made, which leaves the results

uncalibrated, though identifiable approximate periods of 15 minutes and 6 minutes are suggested in the 30-minute record that is shown. The microphone used became directionally sensitive at 38 kHz, and because they observed strong directional sensitivity in the noise recorded in the river, Anderson suggested that the frequencies generated by moving sand are dominated by frequencies greater than 38 kHz.

Richards and Milne [1979] further modified the Anderson detector using integrated circuit design and allowed for gain adjustment in the amplification circuits. They also included an octave band-pass filter system to examine the frequency spectra generated, though they were only able to do so in the lab, and at the expense of increasing the amplification gain. They tested the system at two field sites and in the flume. The two field sites had very different size distributions. One sand-bedded, and the other a granule-sand mix. Both sites had maximum sizes of less than 6 mm. Richards and Milne found that although the bedload rating curves of the two sites were very different, the acoustic data could be plotted on the same curve, though with five data points from each site, it is difficult to be certain of this. At the sand-bed site, Richards and Milne were able to compare transport and transducer current output over nearly two orders of magnitude. At the coarser site, they were only able to collect data over half an order of magnitude, and the scatter is much greater than for the sand stream, making it difficult to know if the data actually come from the same population. The Richards and Milne flume study indicates that Froude number, as well as discharge, may impact the sensor volume. They show clearly that introducing a sand bed into an empty flume drastically changes the acoustic output, and the resulting acoustic signal is much more variable than that from the clean-bedded flume.

Much of the recent development of the self-induced noise detectors has been done in the marine realm, studying the movement of sediments under tidal flows.

Millard [*Millard*, 1976] presented the results of experiments in a rotating drum using glass beads and natural sediment. He explored particularly the dependence of the noise frequency upon the size of the sediment, but did not try to quantify the amount in motion. He performed some theoretical investigations, and rejected the hypothesis that normal mode vibrations of the spheres could cause the frequency peaks that he measured in the drum, although he could not reject the hypothesis that two spheres might vibrate as a dipole to produce the observed signal. He was able to excite vibration in steel spheres by introducing acoustic energy at frequencies similar to those that he observed in the moving drum experiments.

Thorne and others [*Thorne, et al.*, 1983; *Thorne, et al.*, 1984; *Heathershaw and Thorne*, 1985; *Thorne*, 1985, 1986b1986a, 1987; *Thorne and Foden*, 1988; *Thorne, et al.*, 1989; *Williams, et al.*, 1989; *Thorne*, 1993; *Voulgaris, et al.*, 1994, 1995] began with early work in the laboratory, where they put glass spheres in a rotating drum, the inner surface of which was roughened with attached spheres. Thorne then recorded the sound generated as a function of number of spheres and drum speed, to simulate different transport rates. Thorne then compared the results from the laboratory to a theoretical derivation based upon the Hertz Law of Contact, using relationships originally derived by Goldsmith, Koss and others [*Koss and Alfredson*, 1973; *Koss*, 1974; *Akay and Hodgson*, 1978b; *Goldsmith*, 2001]. The theoretical results led Thorne to establish a relationship between the centroid frequency of the broadband spectrum expected from the collision of two particles and the particle sizes. This relationship was tested against mixed-size

artificial sediments in the rotating drum, and was shown to have some predictive power to recreate the size distribution from the acoustic data. Finally, a field platform was used to test the results in the Solent, where agreement of the acoustic signal with video recordings and with Doppler velocimeter data led the authors to conclude that the second-scale temporal variability of gravel transport is dominated by turbulent bursting events.

Other passive acoustic technologies

Govi et alii [1993] installed velocimeters (geophones) in the banks of a stream, and embedded in the bottom sediment immediately upstream from a concrete weir. The original data were recorded on magnetic tape, using frequency modulation to allow for simultaneous recording of the signal from multiple geophones. The data from the bank-mounted geophones had signal-to-noise ratios too small to extract useful information. However, the sediment-embedded geophone produced useable data, which were subsequently sampled at 200 Hz. These data were analyzed to produce, for each minute of record, an average velocity and a count of the number of impacts that exceeded a predetermined threshold. Govi et alii recorded discrete sediment pulses, and were able to establish discharges that correspond to initiation and cessation of motion. Results from the geophone were not compared with results obtained with any traditional sampling technique. One point that was not addressed in this study was whether the positioning of the geophone immediately upstream of the weir was significant. If the velocities measured were induced by material impacting on the weir, then this technology belongs in the class of instrument-induced noise detectors, with the weir included as part of the

instrument. Otherwise, if the velocities are induced by collision of bedload with the sediment in which the geophone was buried, then this instrument belongs in the second class, the self-generated noise detectors.

Summary

Although numerous studies have shown the potential for this technology, none has conducted a systematic theoretical analysis, flume, and field study to determine if a passive acoustic method is viable for quantitative monitoring of coarse bedload transport in streams.

Chapter 3

Theoretical Considerations

The acoustic pressure wave created by two grains of sediment colliding in a river, when detected at a remote, underwater location, is a complex function of the material properties of the grains, the shape of the grains, the geometry of the collision, the geometry of the riverbed, and the relative position of the observation location. In order to render this problem tractable, the assumption will be made that the sediment grains are spherical. This is, in practice, a poor assumption, but it will give a starting point for theoretical analysis.

This chapter will examine two pathways for the generation of sound from the collision of bodies in a fluid. The first is normal mode vibration, in which resonance within the body, excited by elastic deformation of the body during collision, induces propagating pressure waves in the fluid. Because the motion is perpendicular to the grain surface (which is assumed spherical), the efficiency of sound generation will be greatest for the lowest order spheroidal mode, often called the “breathing” mode. Therefore, this mode is of particular interest. The second pathway can be termed rigid-body radiation, in which pressure waves in the fluid are caused by rapid changes in velocity of a rigid body. When a rigid body decelerates, high pressure develops as entrained fluid piles up against the trailing side of the body, and low pressure similarly develops on the leading side of the body. This peak and trough then propagate away from the body as a wavelet.

Breathing Modes

The analysis of the breathing modes of spheres in a viscous matrix has been done many times. The analyses by Ovsyuk and Novikov [1996], Alcalde et alii [2000], and Murray [2002] are followed here. If a sediment grain is considered as an isotropic elastic sphere with radius *a*, density ρ, and Lamé parameters λ and μ, then the equations of motion can be expressed as in Eq. 3.1, where $\vec{\mathbf{u}}$ is the vector velocity of the sphere surface.

$$(\lambda + 2\mu)\nabla(\nabla \cdot \vec{\mathbf{u}}) - \mu\nabla \times \nabla \times \vec{\mathbf{u}} = \rho\partial_t^2\vec{\mathbf{u}} \qquad \text{Eq. 3.1}$$

Because we are only interested in the breathing mode, which has purely radial displacements, this implies that $\nabla \times \vec{\mathbf{u}} = 0$, which implies that $\vec{\mathbf{u}}$ is the gradient of a scalar field, which will be denoted by Φ. Using this information, Eq. 3.1 can be simplified as shown in Eq. 3.2.

$$(\lambda + 2\mu)\nabla^2\Phi = \rho\partial_t^2\Phi \qquad \text{Eq. 3.2}$$

The radial breathing mode solution to this equation, at radius *r* from the center of the sphere, is given by Eq. 3.3, where $j_0(x)$ is the spherical Bessel function of the first kind of order 0, $j = \sqrt{-1}$, ω is the angular frequency of vibration, and c_p is the compressional wave velocity within the sphere: $c_p = \sqrt{\rho^{-1}(\lambda + 2\mu)}$.

$$\Phi = e^{-j\omega t} j_0\left(\frac{r\omega}{c_p}\right) \qquad \text{Eq. 3.3}$$

This simple case of the $j_n(x)$ function can be exploited to simplify Eq. 3.3 as shown in Eq. 3.4 .

$$\Phi = \frac{c_p e^{-j\omega t}}{r\omega} \sin\left(\frac{r\omega}{c_p}\right) \qquad \text{Eq. 3.4}$$

The gradient of Φ has only a radial component, by construction, and can be expressed as in Eq. 3.5.

$$\nabla\Phi = u_r = \frac{1}{r}\left[\cos\left(\frac{r\omega}{c_p}\right) - \frac{c_p}{r\omega}\sin\left(\frac{r\omega}{c_p}\right)\right] e^{-j\omega t} \qquad \text{Eq. 3.5}$$

The boundary conditions require that the surface pressure be equal to the negative of the radial component of the surface stress tensor, at $r = a$. This condition, together with the above results, gives the expression for the surface pressure given in Eq. 3.6 .

$$P = e^{-j\omega t}\left\{\frac{c_p(\lambda + 2\mu)}{a\omega}\sin\left(\frac{a\omega}{c_p}\right) + \mu\left(\frac{2c_p}{a\omega}\right)^2\left[\cos\left(\frac{a\omega}{c_p}\right) - \left(\frac{c_p}{a\omega}\right)\sin\left(\frac{a\omega}{c_p}\right)\right]\right\} \qquad \text{Eq. 3.6}$$

The radial velocity of the spherical surface is given by Eq. 3.7 .

$$\begin{aligned} v_r = \dot{u}_r &= \partial_t\left(\frac{1}{r}\left[\cos\left(\frac{r\omega}{c_p}\right) - \frac{c_p}{r\omega}\sin\left(\frac{r\omega}{c_p}\right)\right] e^{-j\omega t}\right) \\ &= \frac{-j\omega}{r}\left[\cos\left(\frac{r\omega}{c_p}\right) - \frac{c_p}{r\omega}\sin\left(\frac{r\omega}{c_p}\right)\right] e^{-j\omega t} \end{aligned} \qquad \text{Eq. 3.7}$$

The specific acoustic impedance at the boundary is defined by Eq. 3.8. [*Kinsler and Frey*, 1962]

$$z_f \equiv \frac{P}{v_r} \qquad \text{Eq. 3.8}$$

Combining Eq. 3.6, Eq. 3.7, and Eq. 3.8, we get an expression for the breathing mode oscillation frequency, ω (Eq. 3.9), where c_s is the velocity of transverse waves in the sphere, and is given by $c_s = \sqrt{\mu/\rho}$.

$$\frac{4c_s^2}{c_p^2} + \frac{a\omega}{c_p^2}\left[\frac{jz_f}{\rho} + \frac{ac_p\omega}{a\omega\cot\left(\frac{a\omega}{c_p}\right) - c_p}\right] = 0 \quad \text{where} \quad j = \sqrt{-1} \qquad \text{Eq. 3.9}$$

For a spherical interface, Kinsler and Frey [1962, eq. 7.20] give the complex specific acoustic impedance as Eq. 3.10, depending on the fluid density ρ_f, the speed of sound in the fluid c_f, the frequency ω, and the radius of the sphere, a.

$$z_f = \frac{\rho_f c_f^2 a\omega}{c_f^2 + a^2\omega^2}\left(\frac{a\omega}{c_f} - j\right) \qquad \text{Eq. 3.10}$$

Substitution of Eq. 3.10 into Eq. 3.9 and the use of an iterative solver allows for the solution of the breathing mode frequency ω. Thorne and Foden [*Thorne and Foden*, 1988], citing Love [*Love*, 1944] (who cites an 1882 paper by Lamb), suggests Eq. 3.11 for the variation of frequency with grain diameter (D). However, the coefficient in this equation is only valid for Poisson solids. It should also be noted that this formulation is applicable only to free grains, unimmersed in fluid.

$$f = 0.816 \, c_p / D \qquad \text{Eq. 3.11}$$

For the purposes to which this equation was put by Thorne and Foden, it is probably accurate enough. However, if accurate predictions of frequency are required, then the assumptions used in its construction must be relaxed. The true equation will depend upon the physical properties of the grain and, to a lesser extent, of the water in which it is immersed. Here, Eq. 3.9 is solved for quartz grains (c_p = 5466 m/s, c_s = 3462

m/s, ρ = 2620 kg/m³) immersed in 9 °C water (c_f = 1442 m/s, ρ_f = 999.8 kg/m³), which yields Eq. 3.12.

$$f = 0.7552 \, c_p / D = 4128 / D \qquad \text{Eq. 3.12}$$

The effect of the fluid on the frequency of oscillation can be assessed by solving Eq. 3.9 and Eq. 3.10 with a fluid density of zero. The sound speed in the fluid can be set to any value but zero (because of computational constraints) without effect on the solution. The resulting coefficient in the frequency equation, Eq. 3.13, differs only slightly (<1%) from that in Eq. 3.12

$$f = 0.7610 \, c_p / D = 4159 / D \qquad \text{Eq. 3.13}$$

Using Eq. 3.12, a spherical quartz boulder with a diameter of 4 m would have a normal mode vibration frequency of 1032 Hz; and a spherical quartz pebble with a diameter of 4 mm would vibrate at about 1.032 MHz. Therefore, depending on the size particles in motion, and the frequencies monitored, the breathing mode mechanism may be an important source of noise in the river; specifically, particles with a diameter greater than about 0.2 m will generate normal mode vibrations of less than 20 kHz, which will be audible to most people, if the amplitude is sufficiently large.

Very large grains will also contribute sound from higher order solutions to Eq. 3.9. There is an infinite series of solutions, which must be solved individually. Table 3-1 shows the first 14 solutions for the coefficients of c_p/D, in Eq. 3.13, for quartz grains in 9 °C water. Above the fourteenth root, even the oscillations of 4-meter boulders are above the 20 kHz cutoff.

Table 3-1: First 14 roots of the radial breathing mode equation for quartz spheres in 9 °C water.

Root	Coefficient to c_p/D	f for D = 2 mm (Hz)	f for D = 4 m (Hz)
1	0.7552	2064000	1032
2	1.912	5225000	2612
3	2.943	8044000	4022
4	3.958	10820000	5408
5	4.967	13570000	6786
6	5.972	16320000	8161
7	6.976	19060000	9532
8	7.979	21810000	10900
9	8.982	24540000	12270
10	9.983	27280000	13640
11	10.99	30020000	15010
12	11.99	32760000	16380
13	12.99	35490000	17750
14	13.99	38230000	19110

Rigid Body Radiation

The radiation of pressure waves from the acceleration of a rigid body in a fluid is due to the compression of the fluid in the direction of acceleration and rarefaction of the fluid in the opposite direction. This effect does not depend implicitly upon a collision, but will occur when any acceleration of a grain relative to the fluid takes place. However, unless the acceleration is large, the resultant pressure fluctuations will be very small, so perceptible sound will only be generated during an impact condition. The production of such sounds can therefore be separated into two problems. First is the acceleration and deceleration of the grains during a collision, which can be approached using the Hertz Law of Contact for elastic collisions. Second, the propagation of the sound into the far-field must be examined.

Hertz Law of Contact

The Hertz Law of Contact (HLC), first described by Hertz in 1881 [*Hertz*, as cited in *Goldsmith*, 2001] as a parallel problem in electrostatics, describes the stress and strain near the contact point as a function of the geometry and elastic properties of the contacting bodies. In the commonly used form, the HLC assumes that both bodies can be approximated as paraboloids in the vicinity of contact, and that the vibrations induced within the bodies can be neglected during the time of collision (i.e. the duration of contact is short compared with the period of oscillation). The following description is a summary of the more complete analysis found in Goldsmith. [*Goldsmith*, 2001]

The general form of the law is a force-deformation relation expressed in Eq. 3.14.

$$F = k_2 \alpha^{3/2} \text{ if } \alpha > 0 \qquad \text{Eq. 3.14}$$

F is the force acting on either body, α is the approach, which in the case of two spheres, is the difference of the distance between the centers of the spheres and the sum of the two undeformed radii. k_2 is a constant dependent on the geometry and elastic properties of the two bodies. For the case of two spheres of radius a_1 and a_2, k_2 can be represented as Eq. 3.15, given the Young's modulus E_i and the Poisson Ratio μ_i for each sphere *i*.

$$k_2 = \frac{4}{3\pi}\left(\frac{1}{\delta_1 + \delta_2}\right)\sqrt{\frac{a_1 a_2}{a_1 + a_2}} \quad \text{where } \delta_i \equiv \frac{1-\mu_i}{E_i \pi} \qquad \text{Eq. 3.15}$$

Integration of this relationship with initial conditions $\dot{\alpha}(0) = v_0, \alpha(0) = 0$ gives a formulation (Eq. 3.16) for the maximum approach (α_m).

$$\alpha_m = \left(\frac{5v_0}{4k_1k_2} \right)^{2/5} \text{ where } k_1 = \frac{m_1 + m_2}{m_1 m_2} \text{ and } m_i \text{ is the mass of grain i} \qquad \text{Eq. 3.16}$$

The functional relationship between time and approach is implicit, and requires the elliptic integral shown in Eq. 3.17.

$$t = \int_0^{\alpha} \frac{d\alpha}{\sqrt{v_0^2 - \frac{4}{5}k_1k_2\alpha^{5/2}}} \qquad \text{Eq. 3.17}$$

From the assumption that the deformation is fully elastic and reversible, the duration of contact must be twice the time to maximum approach (Eq. 3.18).

$$\tau = 2\int_0^{\alpha_m} \frac{d\alpha}{\sqrt{v_0^2 - \frac{4}{5}k_1k_2\alpha^{5/2}}} = \frac{4}{5}\sqrt{\pi}\,\frac{\Gamma\left(\frac{2}{5}\right)}{\Gamma\left(\frac{9}{10}\right)}\frac{\alpha_m}{v_0} \qquad \text{Eq. 3.18}$$

A numerical solution to the HLC is shown in Figure 3-1 , given two quartz spheres of 0.0254 m radius, and an initial velocity of 1 m/s.

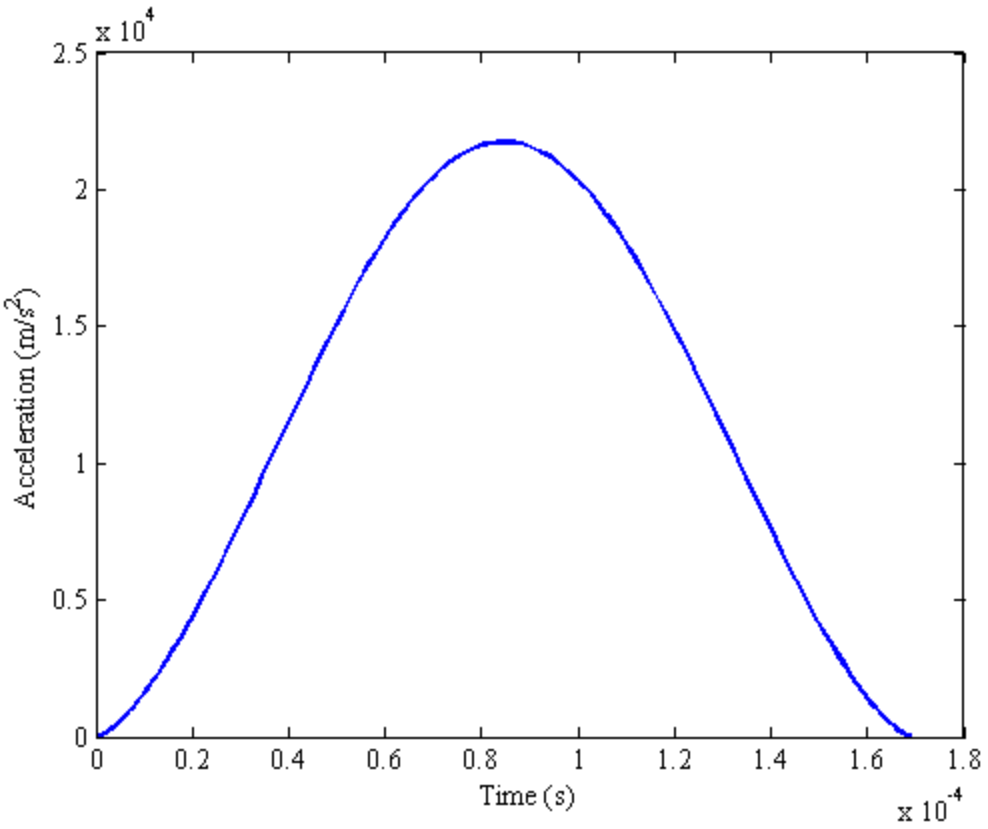

Figure 3-1: Numerical solution to the Hertz Law of Contact, given two quartz spheres of five-centimeter diameter, and an initial impact velocity of 1 m/s.

Hunter suggested an analytical approximation (Eq. 3.19), for *α(t)*, cited in Goldsmith [2001].

$$\alpha \approx \alpha_m \sin\left(\frac{\pi t}{\tau}\right) \qquad \text{Eq. 3.19}$$

The second time derivative of the approach, given in Eq. 3.20, is the relative acceleration of the two spheres.

$$\ddot{\alpha} \approx -\alpha_m \frac{\pi^2}{\tau^2} \sin\left(\frac{\pi t}{\tau}\right) \qquad \text{Eq. 3.20}$$

The integral of the acceleration function over the interval $0 \leq t \leq \tau$ is proportional to the initial velocity of the grain. The constant of proportionality is twice the coefficient of restitution. The assumptions of Hertz's theory imply that the coefficient of restitution should be unity, and in fact, the numerical integration of a variant of Eq. 3.14 gives this result, within numerical precision. However, the numerical integration of Eq. 3.20 does not give this result, but a value of approximately 1.13.

In order to correct this discrepancy, an improved approximation is presented here. First, given the curvature of the numerical solution (see Figure 3-1), a curve of the form of Eq. 3.21 was postulated by this author, where γ is some constant.

$$\ddot{\alpha} \approx \gamma - \gamma \cos\theta \qquad \text{Eq. 3.21}$$

However, this form of the curve overcorrects for the shortcomings of the Hunter/Goldsmith approximation, and so a weighted average of Eq. 3.20 and Eq. 3.21 is shown in Eq. 3.22, where A is the same coefficient used in the Hunter/Goldsmith approximation. ς is a coefficient determined by setting the integral over the interval $0 \leq t \leq \tau$ equal to twice the input velocity, which forces the unit coefficient of restitution assumed by the original theory. Figure 3-2 shows a comparison between the numerical solution to the Hertz contact problem and the two approximations described. κ_1 and κ_2 are the weighting constants, constrained by $\kappa_1 + \kappa_2 = 1$. Fit was made by eye, and the best results were obtained with $\kappa_1 = 0.3$ and $\kappa_2 = 0.7$, and therefore $\varsigma \approx 0.5792$.

$$\ddot{\alpha} \approx \kappa_1 A \sin\left(\frac{\pi t}{\tau}\right) + \kappa_2 \left[\varsigma A - \varsigma A \cos\left(\frac{2\pi t}{\tau}\right)\right]$$
$$A = -\alpha_m \pi^2 \tau^{-2} \qquad \text{Eq. 3.22}$$
$$\varsigma = 2\left[-\kappa_1 \sqrt{\pi}\,\frac{2\Gamma\left(\frac{7}{5}\right)}{\Gamma\left(\frac{9}{10}\right)}\right]\kappa_2^{-1}\pi^{-3/2} \approx \frac{0.3592\left(1.661 - 1.772\kappa_1\right)}{\kappa_2}$$

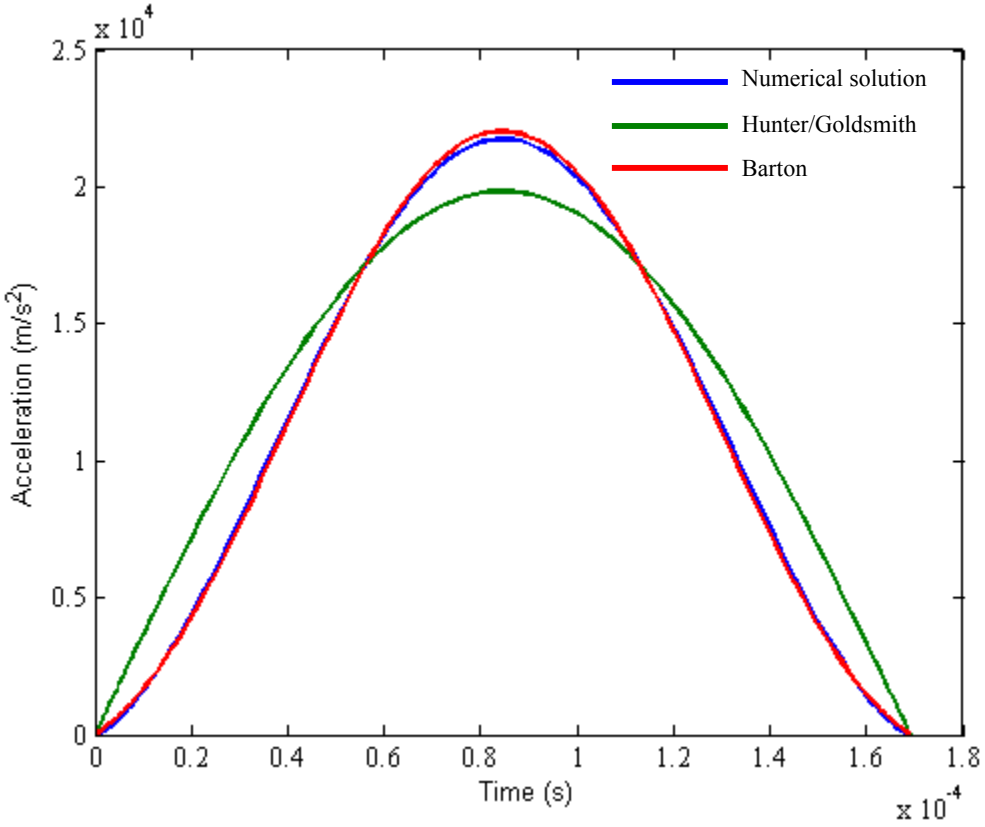

Figure 3-2: Comparison of the numerical solution (blue curve) of Eq. 3.14 with the two approximations described. The green curve is the Hunter/Goldsmith approximation (Eq. 3.20). The red curve is the approximation developed here (Eq. 3.22). The areas under the red and the blue curves are equivalent, both resulting in a coefficient of restitution equal to one, while the area under the green curve is larger, resulting in a coefficient of restitution greater than one. These curves were produced for five-centimeter diameter quartz spheres impacting at 1 m/s.

Radiation of Sound

The far-field sound pressure generated by the unit impulse acceleration was originally described in the 1880s by Kirchhoff [*Kirchhoff*, as cited in *Akay and Hodgson*, 1978], and has been reviewed extensively in the literature [e.g *Koss and Alfredson*, 1973]. The potential function has been shown to be Eq. 3.23, which is Equation 3 from Akay and Hodgson [1978a]. In this equation, a is the radius of the sphere, r is the range from the sphere (center) to the observation point in the far-field, θ is the angle between the impact vector and the observation vector, c_f is the speed of sound in water, ρ_f is the density of water, and t is time. It should be noted that the range (r) is the length of the path traveled by the sound. Therefore, if two bodies are colliding, depending on the geometry of the collision, the range may need to be corrected to allow the sound to travel along the surface of one of the bodies.

$$\Phi(r,\theta,t) = \frac{\rho_f c_f a^2 \cos\theta}{r^2}\left[\left(1-\frac{r}{a}\right)\sin(\lambda\tau)+\frac{r}{a}\cos(\lambda\tau)\right]e^{-\lambda\tau}$$
$$\lambda = \frac{c_f}{a} \qquad \text{Eq. 3.23}$$
$$\tau = t - \frac{r-a}{c_f}$$

This potential amounts to an impulse response of a linear, time-invariant system [see, for example, *Oppenheim, et al.*, 1999, ch. 2]. By convolving this impulse response with an input acceleration, *A(t)*, we can obtain the acoustic pressure history *p(t)* produced by the acceleration in Eq. 3.24, where ξ is a dummy variable.

$$p(t) = \int_0^t \Phi(r,\theta,t-\xi)A(\xi)d\xi \qquad \text{Eq. 3.24}$$

Substituting Eq. 3.23 and Eq. 3.20 into Eq. 3.24, and assuming that the collision is 9 m away and that $\theta = 0$, the far-field acoustic pressure due to the collision of two 2.54-centimeter diameter quartz spheres at 1 m/s is shown in Figure 3-3, and the frequency response of this collision is shown in Figure 3-4. The **M**-shaped curve is caused by the addition of two pulses of opposite polarity, as the two grains are accelerated in opposite directions. Thorne [1986b] has shown that the frequency (in Hertz) of the primary peak can be estimated by Eq. 3.25, given the Young's modulus E, the Poisson Ratio σ, the sediment density ρ, the acceleration due to gravity g and the grain diameter D.

$$f \approx 0.182\left[\frac{E}{\rho\left(1-\sigma^2\right)}\right]^{2/5}\left(\frac{g}{D^9}\right)^{1/10} \qquad \text{Eq. 3.25}$$

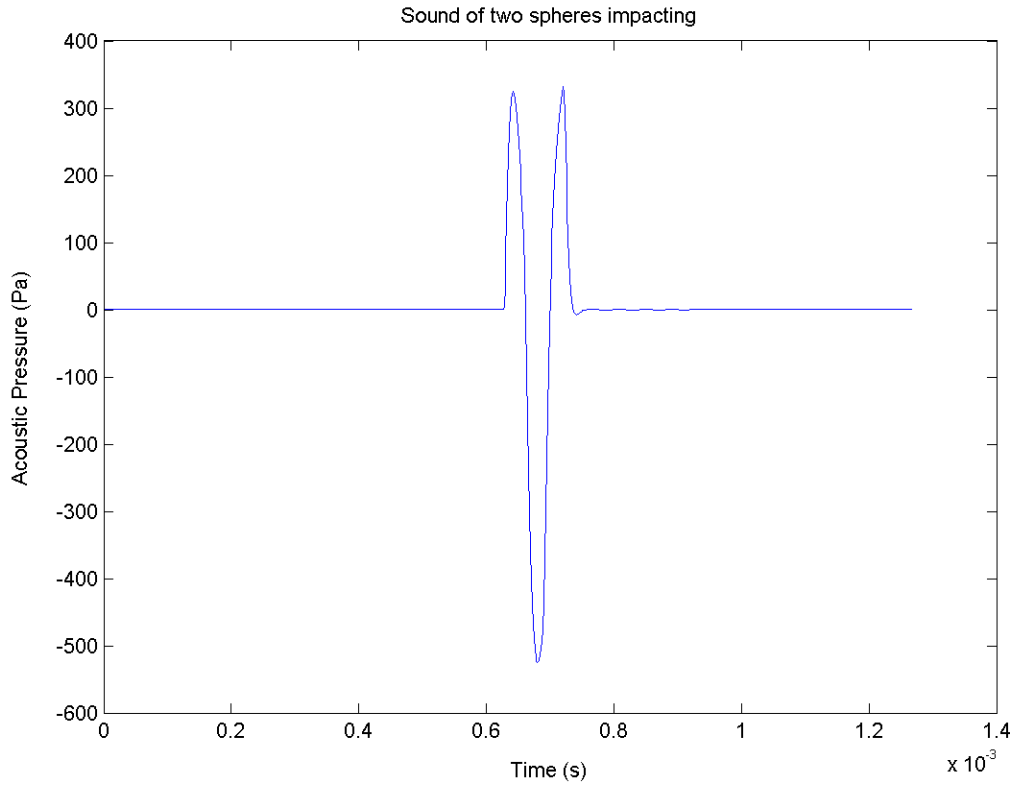

Figure 3-3: Acoustic pressure generated, at a distance of 9 m, and at an angle of 0 radians, by the 1 m/s collision of two 2.54-centimeter diameter quartz spheres. The collision occurs at t = 0.

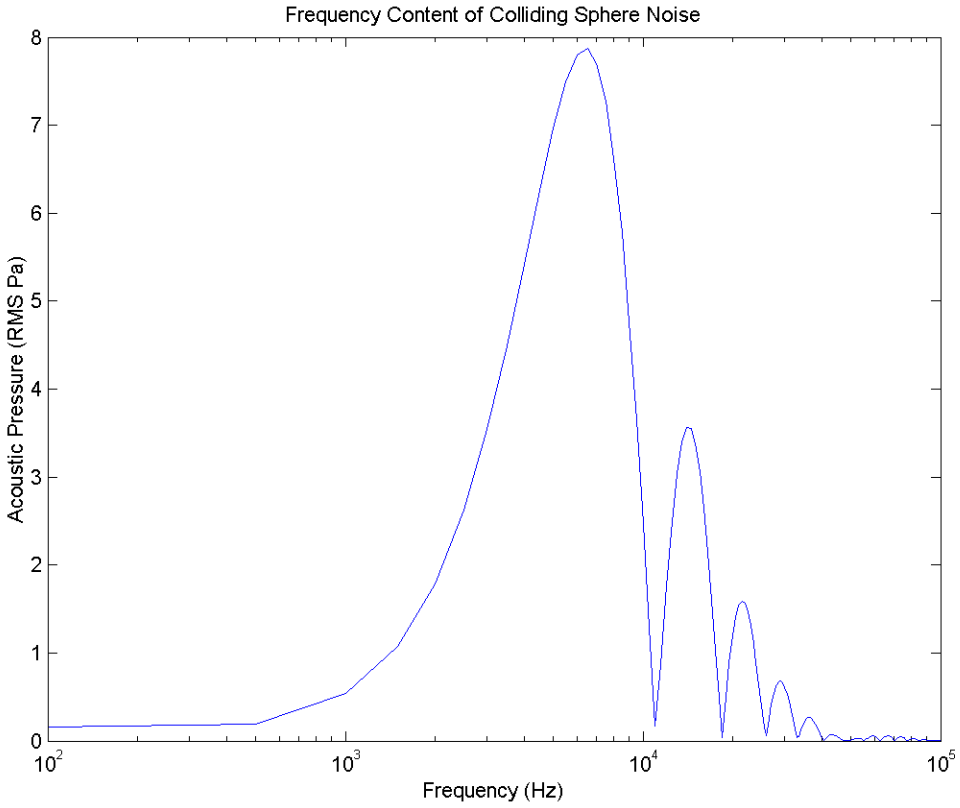

Figure 3-4: Frequency content of the acoustic signal shown in Figure 3-3.

For quartz grains ($E = 7.32\times10^{10}$ Pa, $\sigma = 0.165$, and $\rho = 2620$ kg/m³), Eq. 3.25 can be written as Eq. 3.26.

$$f \approx 220/D^{0.9} \qquad \text{Eq. 3.26}$$

For the 2.54-centimeter diameter grains used in the collision modeled in Figure 3-3 and Figure 3-4, this predicts a peak frequency of about 6000 Hz, which is closely matched by the modeled frequency content.

It is evident from Eq. 3.23 that the response varies with the angle between the observer and the direction of the acceleration. Figure 3-5 shows the dependence of the observed acoustic signal with the angle θ. The signal produced by two spheres is **M**- or

W-shaped, depending on the angle of observation; more specifically, depending on the sign of the cosine of the angle of observation. This dependence upon the angle of observation can also be interpreted as a dependence of the overall signal upon the line-of-sight acceleration, which moves the dependence on the angle from the impulse response to the acceleration function. Therefore, it is not surprising that on the plane perpendicular to the acceleration direction, where the line-of-sight acceleration is zero, the total response is also zero.

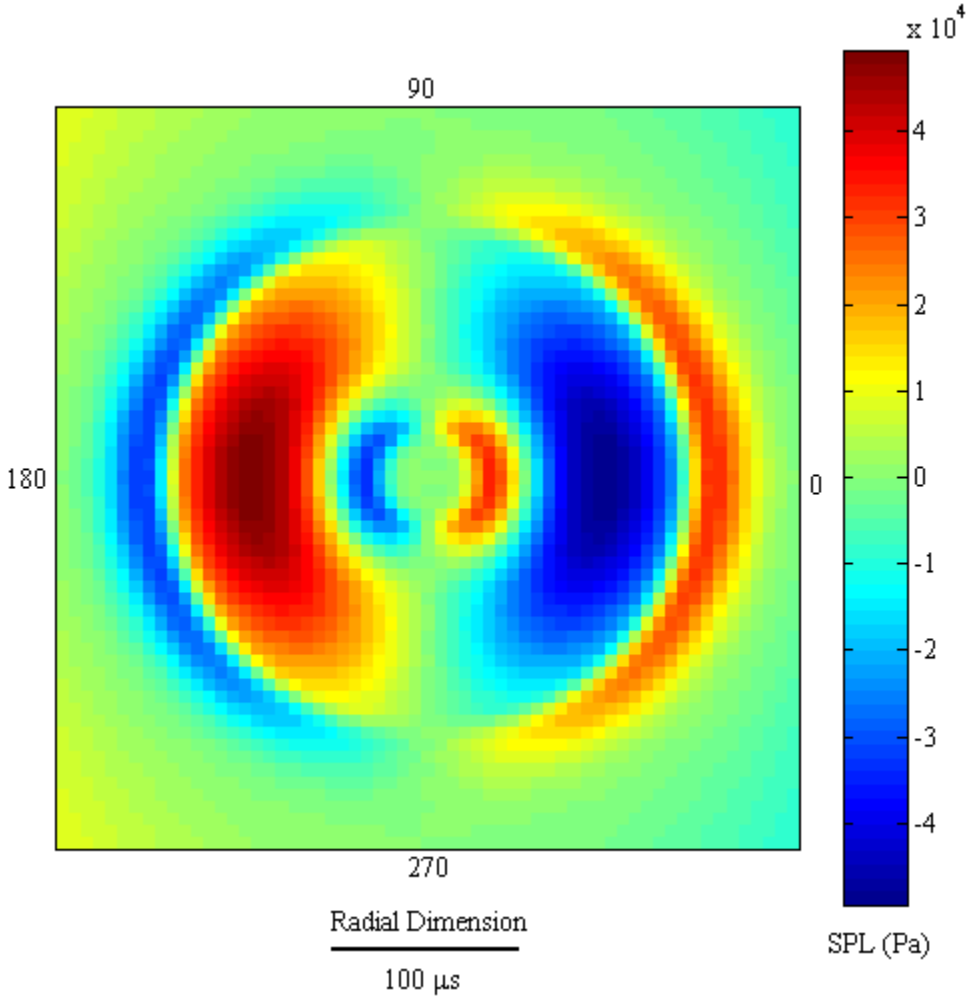

Figure 3-5: Polar plot of acoustic signal versus the azimuth of observation. The radial dimension represents time, and the color represents the pressure level. Azimuth is measured counterclockwise from the positive x-axis, in degrees. The signal shown is due to a collision of two 1-cm-diameter quartz spheres at a distance of 5 cm from the observation point. In three-dimensions, the dependence on azimuth is axisymmetric around the direction of acceleration (in this plot, the line connecting 0 and 180).

Dependence of acceleration and radiated sound upon impact speed

The maximum acceleration ($\ddot{\alpha}_m$) achieved during impact must occur at the moment of maximum approach (α_m), and can be derived by substituting $\alpha = \alpha_m$ into Eq. 3.14. Substitution of Eq. 3.16 into the result gives Eq. 3.27.

$$\ddot{\alpha}_m = k_1 k_2 \alpha_m^{3/2} = \left(\frac{5}{4}\right)^{3/5} (k_1 k_2)^{2/5} v_0^{6/5} \qquad \text{Eq. 3.27}$$

The acceleration amplitude therefore scales with $(v_0)^{1.2}$. Because the impulse response does not depend upon the impact speed, it can be expected that the amplitude of the sound wave produced by the rigid body radiation will also scale with $(v_0)^{1.2}$.

Conclusions

Although floods may move sediment large enough to produce normal mode vibrations within the frequency range of human hearing (assumed to be <20 kHz), only the largest grain sizes will produce sufficiently low frequency tones to overlap the frequencies generated by rigid-body radiation. However, in floods where boulders are moving, it is important to take into account that the rigid-body radiation noise will be mixed with normal modes from the boulders. In cases when only a few large boulders are moving at a given moment, it may be possible to use the normal modes to analyze the motions of these grains.

Breathing mode vibrations produced by coarse material will range from 2.1 MHz for two-millimeter gravel to 1032 Hz for four-meter boulders. Any particle larger than

0.2 m in diameter will produce breathing mode oscillations within the range of human hearing. Very large particles may produce more than one breathing mode oscillation frequency within this frequency range.

Rigid body radiation causes sound to be produced within the range of human hearing for a much larger range of grain sizes. Rigid body radiation produces sound over a broad, continuous range of frequencies, and it is useful to speak of the centroid frequency, which can be thought of as a center-of-mass of the power spectral density function. This centroid frequency ranges from 59 kHz, for two-millimeter gravel, to 63 Hz for four-meter boulders. Thorne and Foden [1988] suggested that the frequency content of the signal diminishes to negligible values above ten times the centroid frequency. This suggests that to capture the entire coarse sediment range, one would need to have hydrophones sensitive between 0 and 590 kHz, and analog-to-digital conversion rate of at least 1.18 MHz, and preferably closer to 1.77 MHz.

The dependence of the amplitude of the sound generated is a 6/5 power of the impact speed. Given impact speeds that should range from near zero (for glancing blows, at least) to something on the order of fluid velocities, approximately 5 m/s, we can expect this to affect the sound amplitude by a factor of 0 to 7. In addition, if increased fluid velocity caused increased mean impact speed, the mean amplitude of the sounds produced by the bedload transport should also increase by the same relationship.

The directionality of the sound generated by rigid body radiation is such that if the mean collision direction is close to vertical, there will be very little energy transmitted parallel to the bed. This suggests that the signal received from collisions near to the sensor, if the sensor is positioned above the collision, should be much louder than the

signal received from a collision at a great distance. In practice, given a natural system with a rough bed, non-planar water-air interface, and turbulent eddies, the paths of the acoustic waves are complex, and reflection and refraction may make this effect much less dramatic than it first appears. In addition, if all of the collisions occur at a distance from the hydrophone, and the angle is always close to zero, then the differences between collision amplitudes will be slight, as the sensitivity to deviations will be small.

Examined here are two mechanisms through which sound will be generated during a collision between sediment grains. Normal mode oscillations, excited by elastic deformation of the colliding bodies, produce generally high-frequency noise that may be difficult to capture for a wide range of sediment sizes. Rigid body radiation produces sounds whose frequency ranges are better situated within the capabilities of lower-cost recording equipment. The scaling of mean amplitude with impact velocity indicates that it may be necessary to include a near-bed fluid velocity measurement to correct for fluctuations in velocity. Directionality of the sound produced in a collision may bias the instrument towards certain geometries of sediment collisions, and multiple instruments may be required to overcome this potential problem.

Symbols

Table 3-2: Symbols used in Chapter 3.

Symbol	Definition	Units
a	grain radius	m
a_i	radius of grain i	m
c_f	speed of sound in fluid	m/s
c_p	speed of percussive waves within the grain	m/s
c_s	speed of transverse waves within the grain	m/s
D	grain diameter	m
E	Young's modulus	Pa
f	frequency	Hz
F	force exerted on one grain by the other	N
g	acceleration due to gravity	m/s²
i	integer grain index in collision problem: $i = \{1,2\}$	
j	imaginary unit, $\sqrt{-1}$	
$j_0(x)$	spherical Bessel function of the first kind, of order 0	
k_1	reciprocal of reduced mass	kg^{-1}
k_2	Hertz Law of Contact constant (see Eq. 3.15)	$Pa \cdot m^{½}$
m_i	mass of grain i	kg
P	surface pressure (normal stress)	Pa
r	radial dimension variable	m
t	time, in seconds. Collision occurs at t = 0.	s
v_0	relative velocity of the grains at the moment of impact ($\alpha = 0$)	m/s
v_r	radial velocity of the surface of the sphere	m/s
z_f	specific acoustic impedance of the grain-fluid boundary: $z_f \equiv P/v_r$	kg/s
α	approach of colliding grains (distance between centers – sum of radii)	m
α_m	maximum approach achieved during collision	m
$\ddot{\alpha}$	relative acceleration of the grains	m/s²
$\ddot{\alpha}_m$	maximum relative acceleration of the grains	m/s²
δ_i	material property constant in Hertz Law of Contact: $\delta_i \equiv \frac{1-\mu_i}{E_i \pi}$	Pa^{-1}
κ_1, κ_2	nondimensional weights used in approximation to Hertz Law of Contact solution: $\kappa_1 + \kappa_2 = 1$	
λ	first Lamé parameter	Pa
μ	second Lamé parameter: shear modulus	Pa
ρ	density of grain	kg/m³
ρ_f	density of fluid	kg/m³
ς	nondimensional empirical constant used to adjust Hertz Law approximation to force the coefficient of restitution to unity	
σ	Poisson ratio	
τ	duration of contact	s
Φ	scalar potential field in breathing mode calculation impulse response function for rigid body radiation	
ω	angular frequency	rad/s

Chapter 4

Instrument Design

The theoretical considerations of the preceding chapter suggest that a hydrophone, receiving acoustic signals within the approximate range of 0-20 kHz, should be able to detect most of the rigid body sound radiation from the collisions of coarse particles from the bed. The following system was developed to exploit this detection for the subsequent prediction of bedload transport rates.

The system used in the experiments described in this dissertation can be divided into three parts: the submerged assembly, including the hydrophone; the amplifier unit, which also includes an anti-aliasing filter; and, the analog-to-digital conversion and data storage units. The separate units are connected using 50-ohm coaxial cable (RG-174), which provides some protection against environmental, electromagnetic noise.

Submerged Assembly

The core of the instrumentation is a Geospace, Ltd. MP-18 hydrophone. This hydrophone is acceleration-canceling, using two piezoelectric membranes that bend in conjunction because of acceleration, resulting in canceled voltages; and in opposition because of pressure variations, resulting in added voltages. The response of the MP-18 is flat only at frequencies less than 1000 Hz. Theory suggests that the hydrophone selected ought to be sensitive to frequencies out to at least 20 kHz, but the lower cost of the MP-

18 makes it an attractive choice, and it is possible that extensive calibration of the hydrophone may enable the use of the nonlinear portion of the hydrophone frequency response.

The hydrophone is placed within a half-meter long, three-inch PVC pipe, as shown in Figure 4-1. The pipe is perforated with thirty ¾ inch holes, in five rings of six holes each. The rings are spaced 0.075 m apart, and are centered on the pipe. The interior of the pipe is filled with 2 cm cubes of heavy-duty artificial sponge foam. This material, while permeable enough to allow the transmission of pressure waves, prevents turbulent currents from impinging upon the hydrophone, which would result in flow noise similar to that produced by wind or breath on an unshielded microphone.

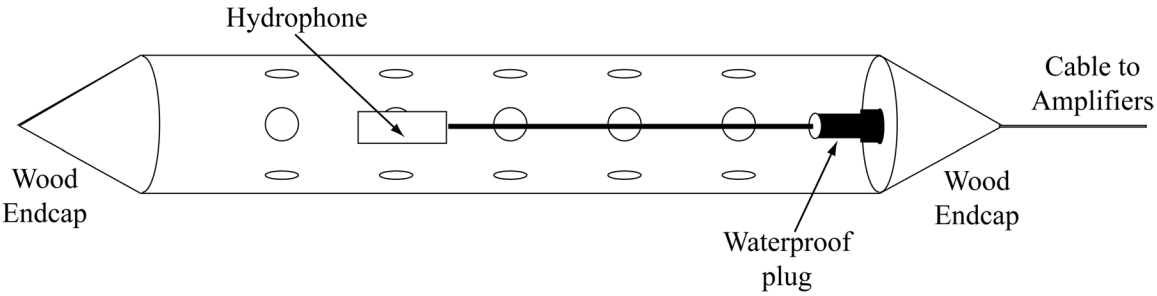

Figure 4-1: Cut-a-way view of submerged assembly. The interior cavity of the assembly is filled with permeable foam blocks (not shown, for clarity). See text for details.

The pipe is capped with conical wooden end-caps, affixed to the pipe with machine screws via threaded taps in the end-caps. The downstream end-cap is drilled out to accept a coaxial cable that terminates on the interior surface of the end-cap in a waterproof receptacle. The coaxial cable connected to the hydrophone is terminated in a waterproof plug that fits into the end-cap. This arrangement allows the end-cap to be removed from the pipe for maintenance without disturbing the hydrophone. The coaxial

cable that exits the pipe through the tip of the downstream end-cap extends above the surface of the water, and terminates in a BNC connector, which attaches to the amplifier described in the next section.

Preamplifier

The preamplifier box should be placed as close to the water as possible, shortening the length of cable between the hydrophone and the box. This cable length varied between the different experiments, but was approximately two meters long. The preamplifier is housed in a cast aluminum box, which must be grounded independently. It would be preferable to place the preamplifier within the submerged assembly, thus minimizing the noise introduced into the system from external fields. Given the difficulties in maintaining a truly waterproof seal while allowing access to replace expended batteries, and the fact that there was little such noise present at the field site used in these experiments, this step was an unnecessary complication for these experiments. It should be noted that there are commercially available hydrophones that include a preamplifier within the housing, which may be a good alternative. These preamplifiers do not typically allow the gain to be adjusted; the importance of this limitation will depend on the specific conditions of use.

The preamplifier circuitry is designed to be a simple, low-gain amplification stage to overcome any noise that might be introduced during transmission of the signal through a long cable to the recording site. The circuit is designed to be simple because of the relative inaccessibility of the box during a data acquisition campaign. It is based on the

Burr-Brown INA141 instrumentation amplifier, in the 10X gain mode (see Figure 4-2). The INI141 amplifier can run on a supply voltage between ±2.25 V and ±15 V; in the experiments reported herein, it was powered by four 9V lithium batteries providing ±9 V.

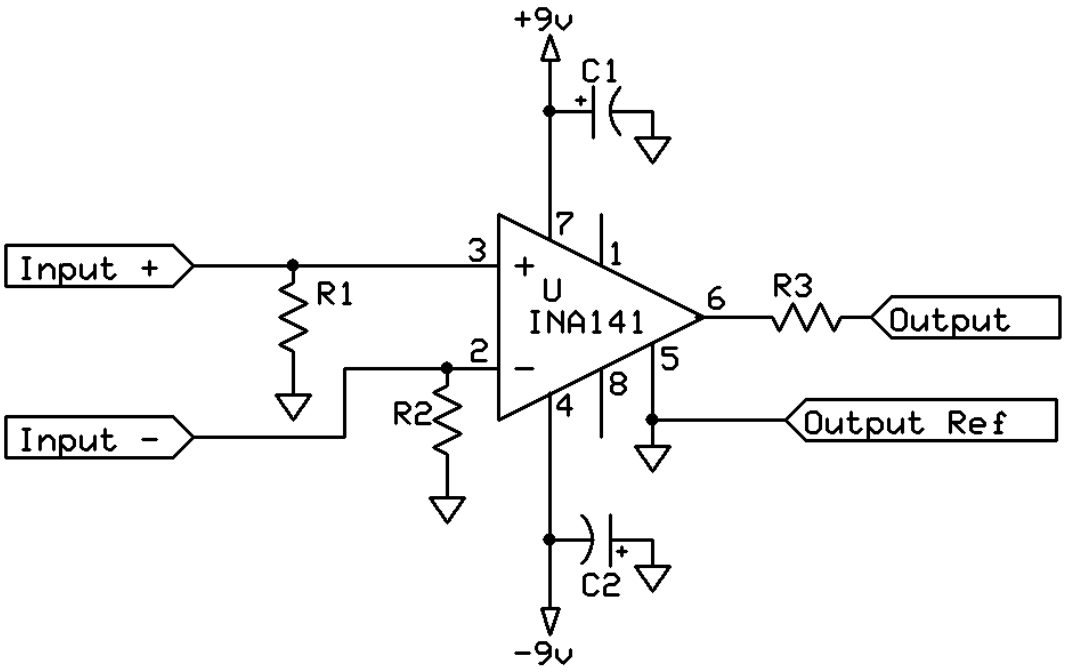

Figure 4-2: Preamplifier circuit diagram. R1=R2=100 KΩ, R3=100Ω, C1=C2=3μF. The output ref is connected to the shield of the coaxial cable, which is connected to the ground of the amplifier circuit in the next stage.

Amplifier and Filter

The cast aluminum amplifier box contains both an amplification circuit (Figure 4-3) and a filter circuit (Figure 4-4). The amplification is achieved using a National Semiconductor low-offset, low-drift dual JFET input operational amplifier: model LF412. This amplifier

allows the adjustment of the gain by placing variable resistance between two pins of the integrated circuit. In this system, the two pins are connected, using a twelve-position rotary switch, to resistors resulting in nominal gains ranging from 1X to 800X. The amplifier is connected to a power supply consisting of two pairs of 9 V batteries connected to deliver 0 and 18 V. A power-regulation unit in the amplifier box splits and regulates the incoming voltage to deliver -5 V, 0 V and +5 V. The 0 V output is at +5 V relative to the incoming 0 V line. These regulated voltages are then passed to the amplifier and filter circuits.

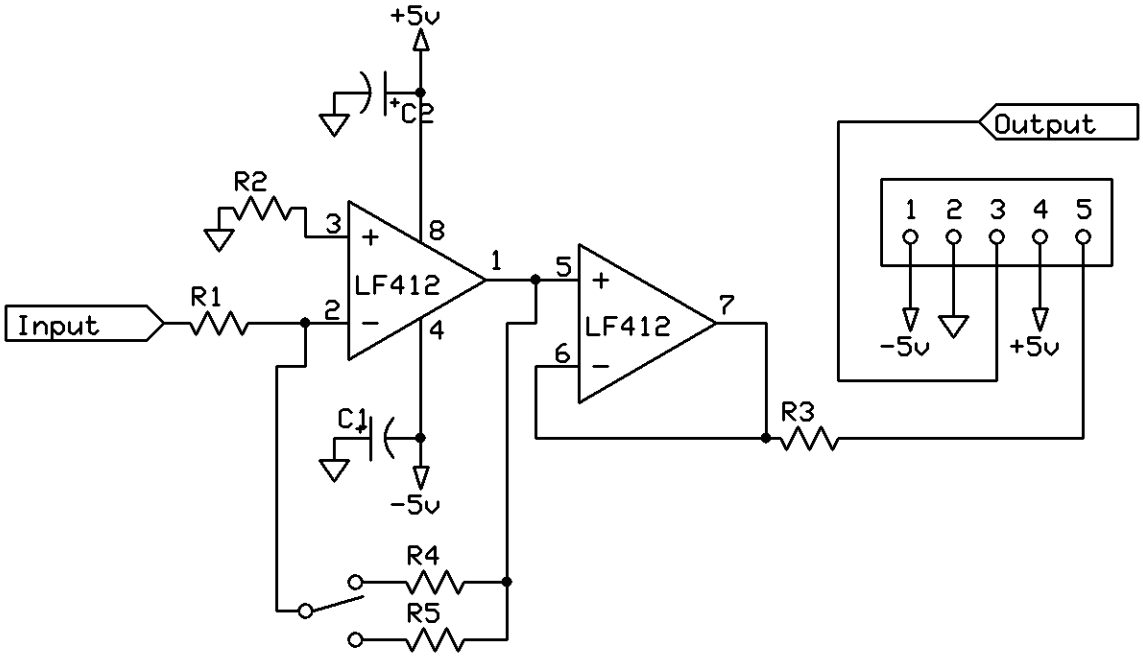

Figure 4-3: Schematic of the main amplifier circuit based on the National Semiconductor LF412. R1=R2=10kΩ, R3=50Ω, R4=3.25MΩ, R5=8MΩ (R4 and R5 were implemented as two series of smaller resistors.); C1=C2=3μF. The five-pin connector shown at far right connects with the filter circuit shown in (Figure 4-4). In the field experiments, the dual-throw switch in this diagram was replaced by a twelve position rotary switch, but the two posts shown are the only ones used during operation. All grounds on this diagram are connected.

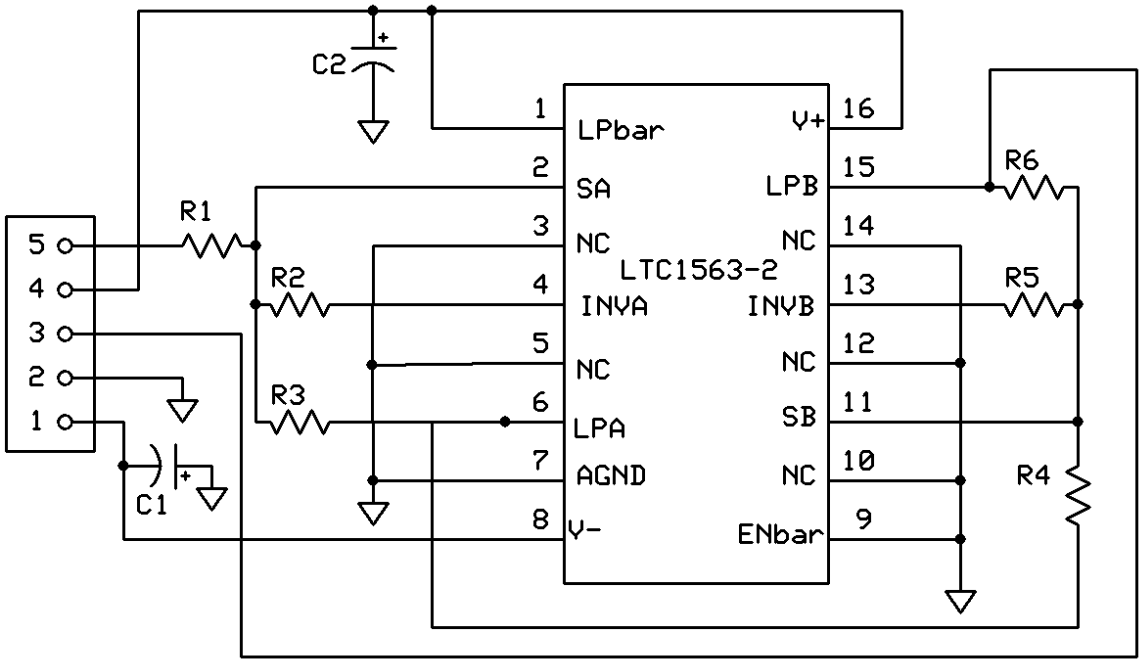

Figure 4-4: Schematic of the analog fourth-order lowpass Butterworth filter, based on the Linear Technology LTC1563-2. The five-pin connector at the left connects with the amplifier schematic in Figure 4-3. All grounds on this diagram are connected.

After amplification, the signal is passed to a Linear Technology active RC, fourth-order lowpass filter: model LTC®1563-2. This integrated circuit design has the transfer function of a fourth-order Butterworth filter, and it is configured to have a cutoff frequency of 22,000 Hz.

The amplifier box is connected to the amplifier and filter ground, and through the coaxial shield, to the computer ground.

Analog-to-Digital Conversion

After amplification and filtering, the hydrophone signal is passed to a National Instruments DAQCard-6036E, a 16-bit PCMCIA analog-to-digital converter for a laptop

computer. The analog-to-digital conversion, sampling the signal at 62,500 Hz, is controlled using The Mathworks, Inc. Matlab Data Acquisition Toolbox. The data are logged directly to hard disk, in the toolbox native format, for one minute, after which a new file is opened, and the process is repeated. This results in nearly continuous operation, with the loss of two to four seconds between each minute of data while the computer performs bookkeeping associated with closing and opening files. This file size is selected for two reasons: First, the time is comparable with those used as bottom times for standard, portable, bedload samplers (e.g. Helley-Smith or BL-84). Second, the file size is small enough (approximately 7.2 Mb) that several copies of the data can be easily manipulated within the physical memory of the computer, thus avoiding time-consuming memory swapping

Chapter 5

Computer Modeling

A model of the total acoustic output by sediment impacts with the bed is presented. The model is stochastic in that it calculates a statistical impact rate per unit area rather than tracking individual particle trajectories through the modeled reach. The geometry of each collision is determined randomly, and the acoustic output is modeled using the Hertz Law of Contact, presented in Chapter 3. This approach has the advantage that it is computationally inexpensive, and therefore can be used to model moderate-sized reaches such as the study area from Chapter 7.

Because the model does not track individual particle trajectories, it will also fail to include bedform development and propagation in the channel; however, it should be possible to extend the model to include such features synthetically to examine their propagation.

Model Development

Assumptions

Bedload is assumed to move entirely by saltation, and saltation is assumed the only important source of sound. This assumption excludes sounds from vibration of grains without net streamwise motion, which will hold except very near the threshold of motion. This assumption also excludes collisions between two moving particles, which

will hold as long as collisions with the bed are much more frequent than collisions between grains, and therefore, as long as bedload concentrations are low. The bedload transport rate is not permitted to vary over the duration of the model run, which is typically about one second. During saltation, grains are assumed to have only vertical and downstream velocity components.

The cross-section of the river channel is assumed rectangular, and the banks are assumed to play no role in sediment transport. All sediment, both bedload and bed material, is assumed to be spherical, and of a uniform material. The sediment exposed at the surface of the bed is assumed to have the same size distribution as the grains in transport, and the distribution of the bed grains does not change with time. Cross-stream variability in bedload transport rate, when used, is obtained by controlling the availability of sediment, rather than the bed shear stress. The distribution of sediment in movement is assumed constant over the cross-section.

Grains impacting the bed more than one river width upstream or downstream of the measurement location are assumed to have negligible effect upon the acoustic record. For the highest frequencies measured, this corresponds to about 1000λ. This is an arbitrary cutoff, and it may not be applicable to narrow streams.

Saltation

Sklar and Dietrich [2004] derived a saltation model for a single grain size. Extrapolating on this model for a given size class *i*, gives Eq. 5.1 for the rate of impacts per unit time and per unit area, where g_s is the bulk mass transport rate per unit width, P_i

is the percentage of the sediment within the size class, ρ_s is the sediment clast density, D_i is the mean particle diameter for the size class and Λ_i is the mean saltation length for the size class.

$$I_i = \frac{6 g_s P_i}{\pi \rho_s D_i^3 \Lambda_i} \qquad \text{Eq. 5.1}$$

Requiring the knowledge of q_s and P_i, the only remaining unknown is Λ_i. Sklar and Dietrich presented Eq. 5.2 for the saltation length (Λ) of a grain of diameter D, whose denominator allows the hop length to approach infinity as the shear velocity (U_*) of the flow approaches the fall velocity (w_f) of the grain, to mimic suspension. τ_* is Shields' nondimensional shear stress, τ_{*c} is the critical Shields' stress. τ_{*k} is the hiding-corrected critical Shields' stress after Komar [1987], given in Eq. 5.3, where ${}_{50}\tau_{*c}$ is the critical Shields' stress for the D_{50} grain size.

$$\Lambda = D \frac{8\left(\tau_* / \tau_{*c} - 1\right)^{0.88}}{\left(1 - \left(U_* / w_f\right)^2\right)^{1/2}} \quad \text{for} \quad \frac{U_*}{w_f} < 1 \text{ and } \tau_* / \tau_{*k} > 1 \qquad \text{Eq. 5.2}$$

$$\tau_{*k} = {}_{50}\tau_{*c}\left(\frac{D}{D_{50}}\right)^{-0.68} \qquad \text{Eq. 5.3}$$

In the model, the cumulative size distribution provided by the user, presumed based upon a sieve analysis of a known sample, is fitted to a piecewise hermite spline interpolant, which enforces the monotonicity of the cumulative size distribution. This spline is then used to break the size distribution into n smaller bins, and the mean impact rate over the sieve bin is calculated by Simpson's Rule. n is increased and the rate is

recalculated, and this is repeated until the mean impact rate no longer changes by a significant amount.

The bed is divided into a 1 m by 1 m grid, and for each grid cell, a number of collisions calculated using Eq. 5.1 is determined for each size distribution. The number of collisions is rounded off to an integer probabilistically.

Collision Geometry

For each collision, an impactor grain radius is determined using the spline interpolant to the size distribution; and an impactee grain radius is determined using an area-weighted size distribution, making it more likely that a large grain will be impacted than a small grain.

The downstream velocity of the impactor is taken as the mean downstream saltation velocity from Sklar and Dietrich, which is given in Eq. 5.4, where: g is the acceleration due to gravity, D is the diameter of the impactor, τ_* is the Shields' stress on the impactor, and τ_{*c} is the critical Shields' stress for the grain uncorrected for hiding. R_b is the nondimensional buoyant density: $R_b \equiv \rho_s/\rho_w - 1$. The assumption that the velocity of the impactor, at the moment of impact, is equal to the mean saltation velocity is likely to underpredict the actual velocity, as fluid drag will tend to increase the velocity over the entire saltation.

$$\bar{u} = 1.56\sqrt{R_b g D}\left(\frac{\tau_*}{\tau_{*_c}} - 1\right)^{0.56} \qquad \text{Eq. 5.4}$$

The vertical impact velocity (w_I) is also taken from Sklar and Dietrich, who give Eq. 5.5 as an estimated vertical impact velocity, using symbols already described.

$$w_I = 0.8\sqrt{R_b g D}\left(\frac{\tau_*}{\tau_{*_c}} - 1\right)^{0.18}\sqrt{1 - \left(U_* / w_f\right)^2} \qquad \text{Eq. 5.5}$$

The impact pitch, φ, is a random variable that can vary over the range $\tan^{-1}\left(w_I / \overline{u}\right) \le \varphi \le \pi/2$. The impact azimuth, θ, is also random, and can vary over the range $-\pi < \theta \le \pi$. A position within the grid cell is chosen randomly for the collision, under the assumption that the transport is uniformly distributed over the cell. The impactor velocity given by $\overline{u}\hat{i} + 0\hat{j} - w_I\hat{k}$ is then projected along the vector determined by the impact pitch and azimuth, and the random position, resulting in the relative velocity between the impactor and the impactee. The vertical position for the collision point is determined by the impact pitch and the radius of the impactee. A random time is selected for the collision within the recording interval.

Sound Generation

One or more virtual hydrophones are established (in the experiments presented here, there is only one, always placed at the origin) before the model begins, which allows the relative position of each collision to be established and an impulse response based on the range and line-of-sight angle to be determined using Eq. 3.23.

The acceleration of the impactor is calculated using the weighted average approximation to the Hertz Law of Contact presented in Chapter 2 (Eq. 3.22), using κ_1 =

0.3 and $\kappa_2 = 0.7$. For the purposes of the model, the impactee is assumed immobile, and this is modeled in these equations by assigning infinite mass to the impactee. The acceleration is then convolved with the impulse response for each hydrophone. This result is sampled at a much higher frequency than the desired output. The result of the convolution is then transformed into the frequency domain and is passed through both an attenuation filter, which models the differential attenuation with frequency in fresh water, and an anti-aliasing, low-pass filter that matches the analog filter used in Chapters 6 and 7. Following this step, and transformation back into the time domain, the result is downsampled to the desired output frequency, and added to the cumulative record for the virtual hydrophone.

Results and Discussion

The model was driven in three separate experiments using Graham Matthews and Associates' sediment data from the 2005 field campaign. Bedload transport rates and associated sediment size distributions were used, and hydraulic conditions were established such that the largest bedload particle collected was approximately at the threshold of motion. In order to speed processing, for many of the runs, the transport rates were decreased while keeping the sediment size distributions and hydraulics constant.

Dependence of Acoustic Power upon Transport Rate

In order to examine the relationship between acoustic power and bedload transport rate, the variable of sediment size distribution was eliminated. Seven runs were completed spanning an order of magnitude of transport rates, using a common sediment size distribution (no sediment finer than 5.6 mm was included). Figure 5-1 shows the modeled relationship between acoustic power and bedload transport rate; assuming linearity, these variables have Pearson's R = 0.996, with a random correlation probability of 2.49×10^{-6}.

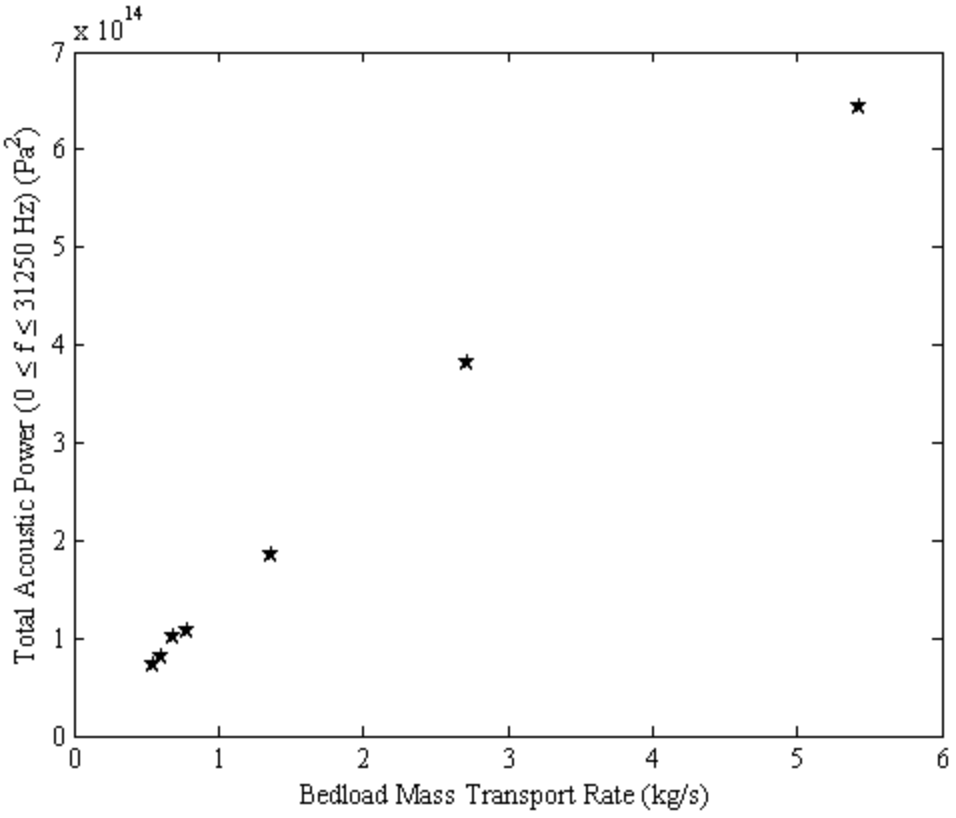

Figure 5-1: Integrated simulated acoustic power (numerical integral of the power spectral density over frequency) as a function of transport rate. All samples have the same size distribution.

Although linearity cannot be rejected over this range of transport rates, (by comparing R^2 for the linear relation with that for a power law $P=x^{\alpha}$, for $\alpha = 0.99$), the relationship does appear to have a power slightly less than unity. This appearance is based upon a single point, however, but may be consistent with results observed in the flume, and described by Jonys and others [e.g. *Jonys*, 1976]. In the model, each particle impacts the bed in isolation, and no interparticle collisions are modeled. It is possible that at high sediment concentrations, interparticle collision noise will become more important than particle-bed interactions, and a different acoustic model will be necessary.

The simplification with respect to sediment size distribution was relaxed, so that for the observed transport rates in the GMA data, corresponding observed sediment size distributions were also used, and Figure 5-2 shows the modeled relationship including all runs. It is evident that the linearity of the relationship does not change a great deal (Pearson's R = 0.994, random correlation probability: 6.77×10^{-9}), though there is certainly additional spread to the data.

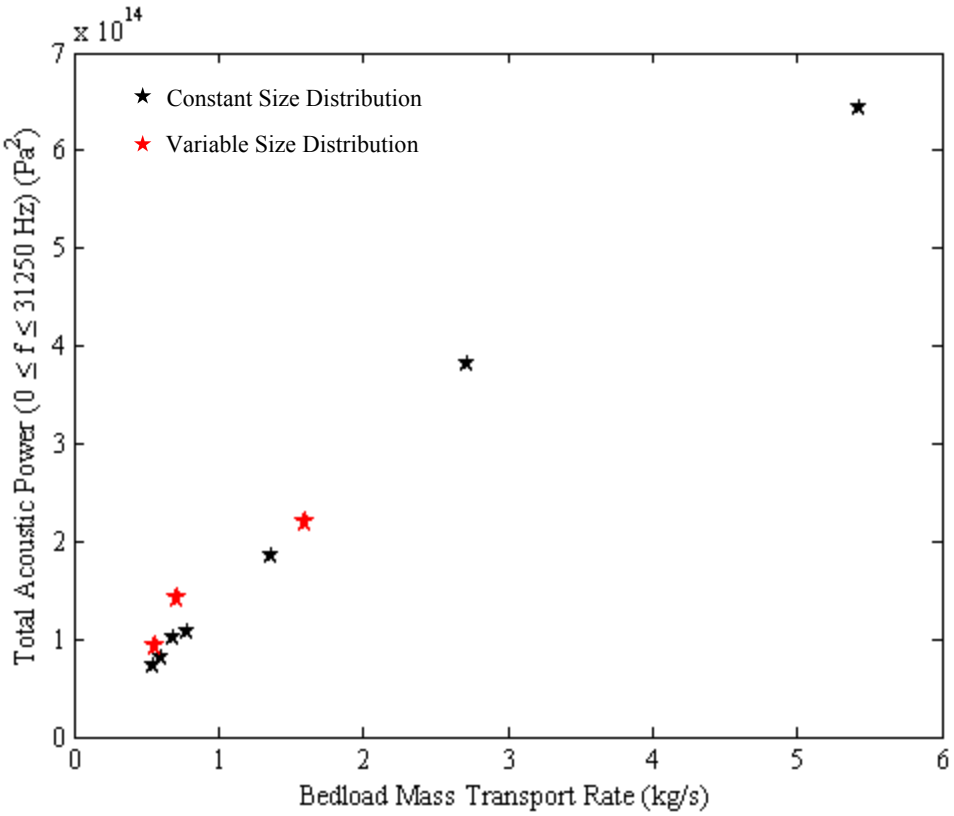

Figure 5-2: Integrated acoustic power (numerical integral of the power spectral density over frequency) as a function of bedload transport rate including points with different sediment size distributions. Variable size distributions were based on field measurements (see Chapter 7).

Spatial Distribution of Sediment Transport

It is also possible to examine the impact of a changing spatial distribution of bedload transport. Two cases were considered. In the first, the rate of bedload impact for size class i was considered to be uniform across the entire channel width and given by Eq. 5.6 , where I_{ij} is the number of impacts per second in cell j of grains in size class i, L_j

is the streamwise length of the cell, W_j is the cross-stream width of the cell, and I_i is the impact rate per unit area for grains of size class *i* calculated from Eq. 5.1.

$$I_{ij} = L_j W_j I_i \qquad \text{Eq. 5.6}$$

In the second, the impact rate of size class i for a given cell *j* was given by Eq. 5.7, where, W_R is the width of the river, w is the cross-stream distance, and w_{jl} and w_{jr} are the cross stream locations of the left and right edges of cell *j*.

$$I_{ij} = I_i L_j W_R \left(\frac{2}{W_R} \int_{w_{jl}}^{w_{jr}} \frac{1}{2} \left[1 - \cos\left(\frac{2\pi w}{W_R} \right) \right] dw \right) \qquad \text{Eq. 5.7}$$

Given $W_j = w_{jr} - w_{jl}$, this simplifies to Eq. 5.8.

$$I_{ij} = I_i L_j \left\{ W_j + \frac{W_R}{2\pi} \left[\sin\left(\frac{2\pi w_{jl}}{W_R} \right) - \sin\left(\frac{2\pi w_{jr}}{W_R} \right) \right] \right\} \qquad \text{Eq. 5.8}$$

This simulates a stream with most of the bedload transport occurring along the centerline. In all comparisons between the two configurations, the total bedload flux through the cross-section was equal. However, it is worth noting that the assumption is made that the size distribution of grains is constant across the channel.

The results of the power spectral denstity over the range 0-2000 Hz are shown in Figure 5-3. The total power derived by integrating the power spectral density over this range shows a difference between the two runs of 1.6 orders of magnitude.

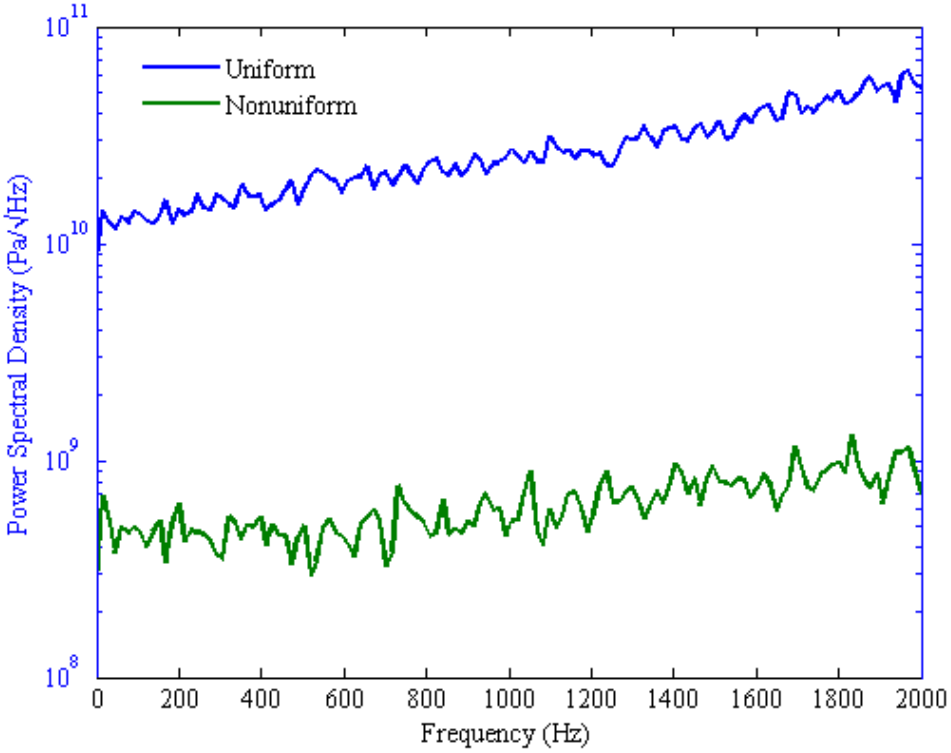

Figure 5-3: Low-frequency power spectral density of two model runs having differing spatial distributions of impacts. The blue power spectral density is due to a uniform distribution of bedload impacts over the entire riverbed. The green power spectral density is due to the nonuniform distribution of bedload impacts where most collisions are near the center of the river (see text for details of distribution). Total bedload transport rate through the cross-section (kg/s) is constant between these two runs. The model hydrophone is located on one bank of the modeled river. Using the entire frequency range modeled does not change these results.

This experiment shows that a single hydrophone should be very sensitive to the change in cross-stream distribution of bedload transport. This is important, as it limits the applicability of calibration relations to periods over which the channel is geomorphically stable. It may also make nonlinear the relationship between bedload transport and acoustic power, if the distribution of bedload transport varies, and is correlated with the

transport rate. However, a natural environment, with complex reflections and refractions of the sound field may make this dependence less clear-cut.

Comparison of Model with Field Data

The model was driven (throughout these experiments) using data from the field experiments described in Chapter 7. A comparison was made between the spectral content of the modeled sound and the sound measured in the field, to attempt to validate the model. A direct comparison cannot be made, because, lacking a complete calibration of the hydrophone (a financial limitation), calibrated acoustic pressure data was not available from the field. This comparison is presented in Figure 5-4, and, it should be noted, has many limitations. The model input conditions are restricted to the sediment size distribution and the total sediment flux rate. The sediment flux was assumed to vary across the channel according to the nonuniform distribution described in the previous section. The flow parameters of the river were derived from the sediment size distribution, such that the flow rate is just large enough to move the largest particle moving in the size distribution. Equal mobility is assumed, so that the stationary bed particles are assumed to have the same size distribution as the moving particles. In a river in which the size distribution of the moving particles changes over the course of a flood, this assumption cannot be accurate. In addition, sediment sampling is assumed to be accurate for the derivation of sediment size fractions for the model. Given that the pressure-difference sampler used to collect this data has a 0.3048×0.1524 m wide mouth, it is not inconceivable that particles of similar size or larger may be moving,

unsampled, on the bed of this river. It is also worth noting that the field data presented is an average spectral density over the one hour while the sediment was collected, while the model result is based on a one-second sample only. This explains the difference in scatter between the two curves.

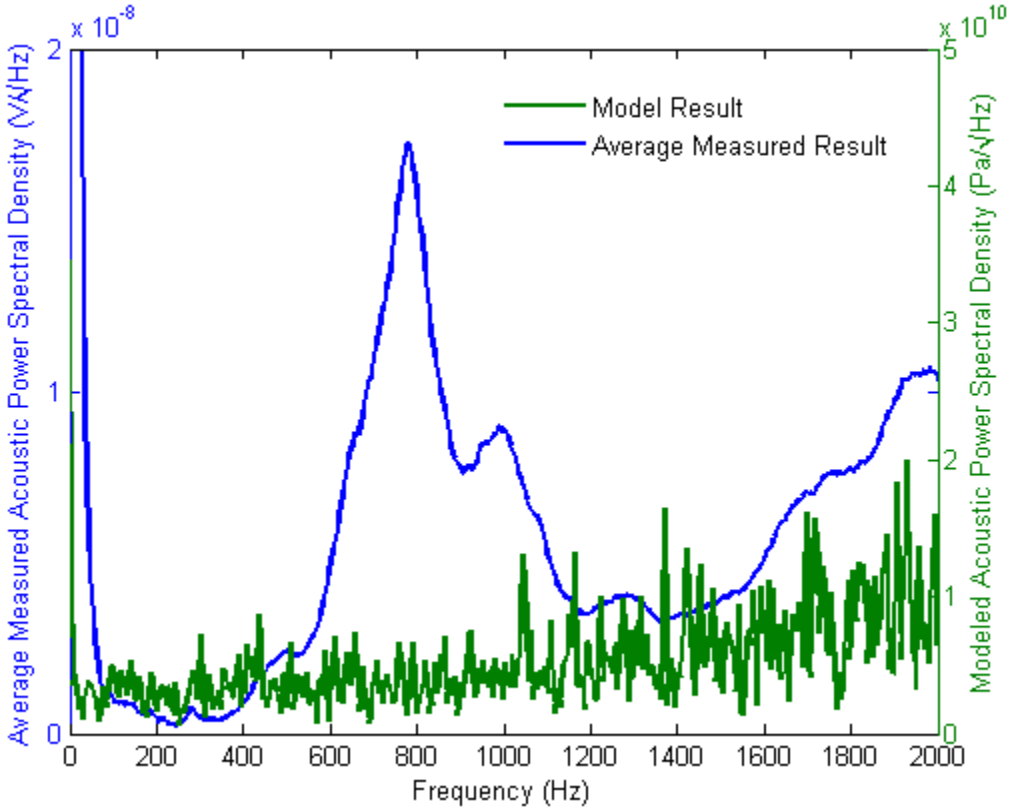

Figure 5-4: Comparison of the model results with measured Trinity River.

There is a large discrepancy in the form of the two datasets, centered primarily on the double peak at 800 and 1000 Hz. Making the assumption that these peaks are due to unmodeled rigid-body radiation, the necessary particles have diameters of 0.24 m (800 Hz) and 0.19 m (1000 Hz). Neither of these sizes seem entirely unrealistic for the flow strengths observed at this field site, and both of them are large enough that they would

not fit into the opening of the pressure-difference sampler. It does seem strange that such a narrow range of sizes should be present in this study reach, however. An alternative, and more likely, explanation is that filtering of the noise by the geometry of the river reach causes acoustic enhancement in this range. Wavelengths in this frequency range are about 1.5-2.5 m, which is also a good description of the water depth in the channel during the time when these data were recorded. More data will be required to investigate this phenomenon further.

Sensitivity to Use of Reduced Frequency Range

The MP-18 hydrophone sensitivity decreases rapidly above about 2000 Hz, well below the theoretical peak frequencies for gravel (see Figure 5-5). It is clear from Figure 5-5 that accounting for the effects of changing size distributions will be difficult using this limited range of frequencies. Thorne and others [e.g. *Thorne*, 1986b] have shown that some size classification of ocean sediments is possible with sufficient high-frequency data, and with a broad-spectrum hydrophone, this may be possible in a fluvial setting as well. However, it was hypothesized that the 0-2000 Hz range would yield sufficient information to make possible the prediction of bedload transport rate.

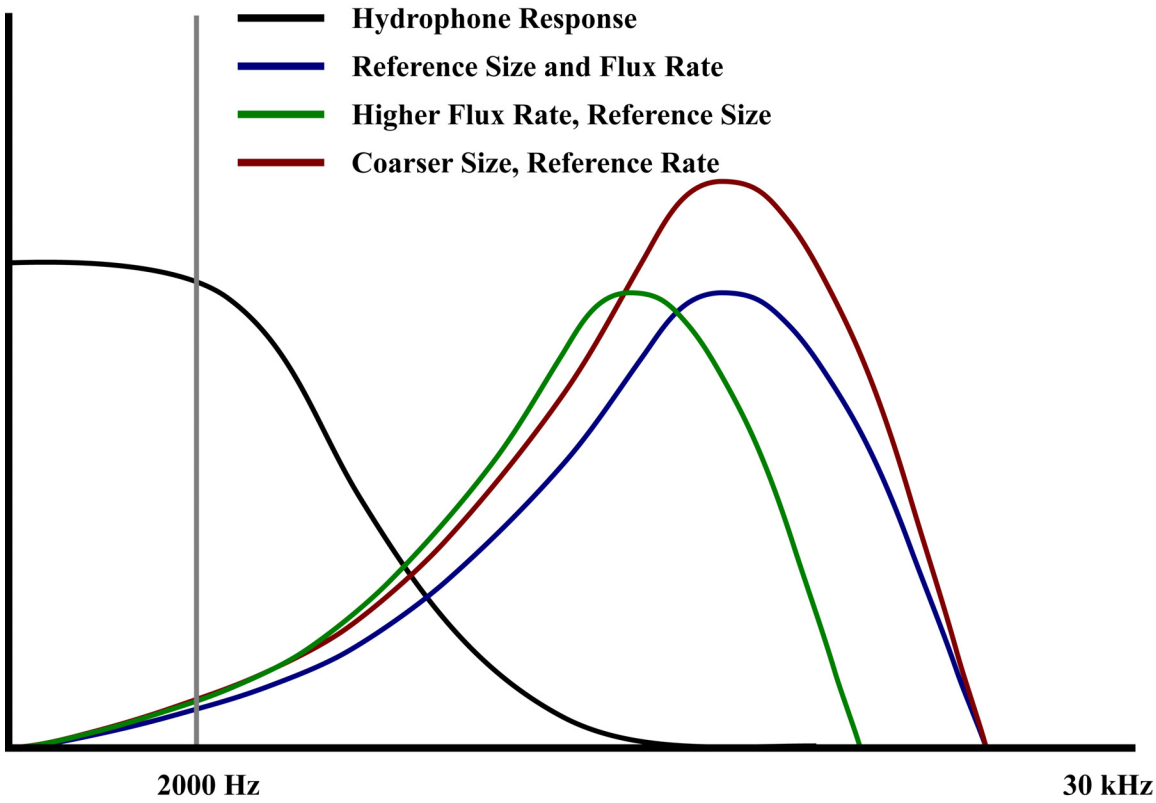

Figure 5-5: Cartoon showing expected frequency spectra of sound from gravel transport compared with the frequency-dependent sensitivity of the hydrophone. This drawing is not to scale.

In order to validate the use of this reduced frequency range, the power spectral density is examined for several different model runs, with different bedload transport rates and with different bedload size distributions.

Given (shown by Thorne and others [*Thorne*, 1986b]) that the frequency content of the received sound is dependent upon the size distribution of the sediment in motion, the test should include that variable. Figure 5-6 shows the power spectral densities of four test runs, whose size distributions are determined from four samples taken at the Trinity River in May 2005 by Graham Matthews and Associates. The distributions were altered for these tests by eliminating the grains finer than 5.6 mm diameter, to speed calculations.

Transport rate estimates were corrected for the eliminated material. Six additional samples were included from model runs used in Figure 5-1, which use the same sediment size distribution as the 0.542 kg/s sample on Figure 5-6.

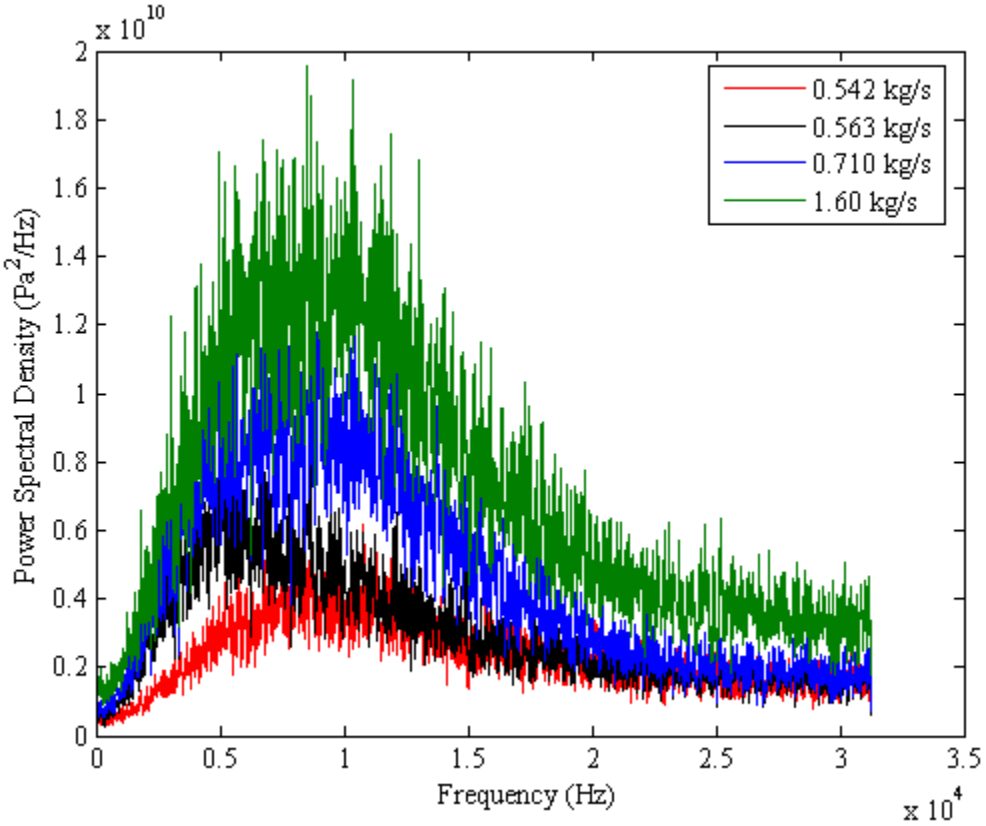

Figure 5-6: Power spectral densities of the four runs used to examine the frequency sensitivity range. Note that, although only the mass transport rate is used to identify the curves in the legend, the sediment size distributions are different for the four samples; the distributions were taken from field data for the corresponding transport rates.

A trapezoidal approximation to the numerical integral is used to calculate the total acoustic power from the power spectral density. Figure 5-7 compares the acoustic power between 0 and 31250 Hz and that between 0 and 2000 Hz.

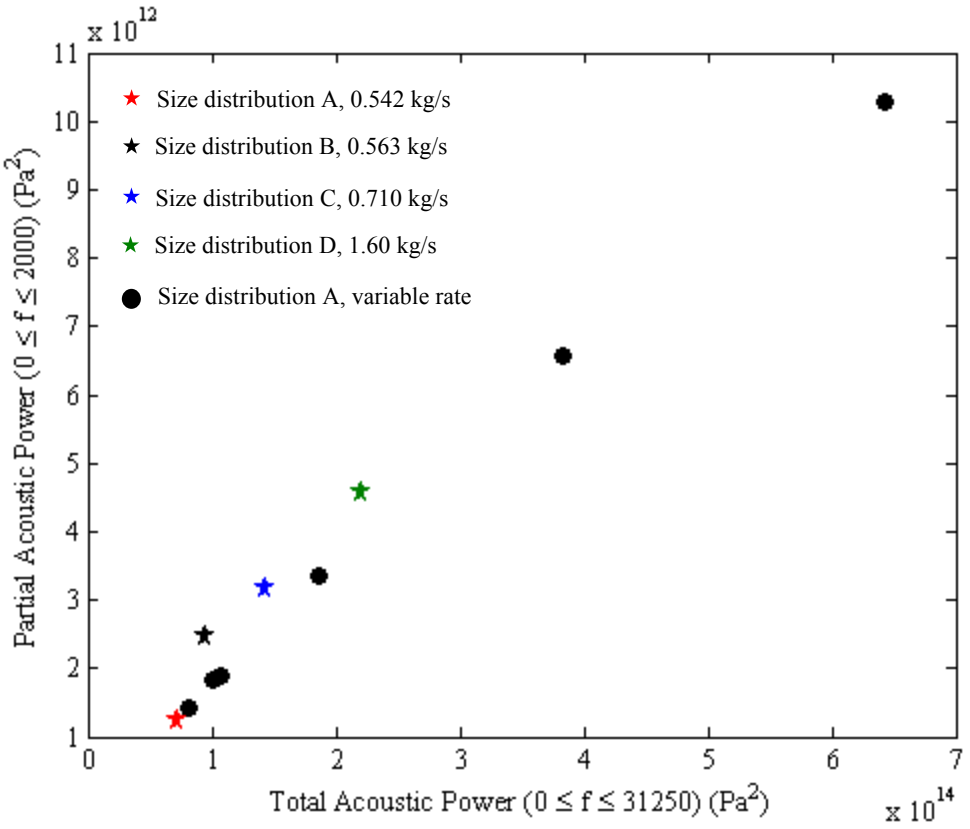

Figure 5-7: Total versus partial acoustic power for runs of varying sediment size distributions and bedload transport rate. Pearson's R = 0.9996, p = 4.0×10^{-4}. The colored pentagrams are matched to the colored curves in Figure 5-6, while the round markers are the additional data described in the text.

The relationship appears linear (Pearson's R = 0.9996, with a random correlation probability of 4.0×10^{-4}). This linearity supports the use of the limited range of frequencies to predict bedload transport rates using hydrophones such as the Geospace MP-18. It is interesting to note that for the data for which the sediment size distribution was stationary, the relationship is more perfectly linear. This suggests that the low-frequency approximation should work better in streams that tend towards equal mobility.

Conclusions

A model has been developed to allow the investigation of the spatial relationships between particle interactions with the bed and the resulting acoustics. Given the assumption that interactions between moving particles are insignificant compared with interactions between moving particles and the bed, the results of the model show a linear relationship between bedload transport rate and total acoustic power. This was established using both a constant size distribution, and by allowing the size distribution to shift with the transport rate.

The model also shows that a single-hydrophone system is extremely sensitive to the location of sediment transport in the cross-stream direction. Calibration of these systems is therefore unlikely to remain valid after channel-forming events. It is therefore suggested that future development include more than one hydrophone, for example, one on each bank at the same cross-section. However, the sensitivity to these changes may be exaggerated by these data. Presented is an extreme case, with a change from an environment where collisions occur regularly less than one meter away to one where the majority of collisions occur ten or more meters away. The sensitivity to change decays with distance, so slight (meter-scale) movements in a thalweg ten or twenty meters from the hydrophone are unlikely to cause this level of uncertainty in subsequent predictions.

Finally, the use of a limited range (relative to the theoretical range for gravel) of frequencies for the prediction of bedload transport was investigated. It was found that the power between zero and 2000 Hz was linearly related to the power between 0 and 31250 Hz, suggesting that it is possible to use this smaller range of frequencies.

Chapter 6

Flume Experiments

In order to observe, in a controlled environment, the acoustic energy generated by colliding sediment grains, several experiments were conducted in a recirculating flume, located in the Department of Civil and Environmental Engineering at Penn State. The experiments were designed to exploit the temporal variability inherent in bedload transport to 1) verify the observations of earlier workers, and 2) establish the functional relationship between total acoustic power and gravel transport rate.

The Flume

The flume used for these experiments was glass-walled, 13.72 m long, 1.524 m wide, and 0.9144 m deep, with an adjustable slope (0–0.0524). The channel was constricted to 0.29 m, using cement-block and plywood, over about 12 m of the flume length. Sand was piled behind the walls to provide additional support. At the downstream end, the channel widened abruptly to the full 1.524 m, to provide a catch-basin for the transported gravel. A 1.9 cm wire mesh baffle inhibited gravel from entering the recirculation system from the catch-basin. Figure 6-1 shows the plan-view of the flume setup.

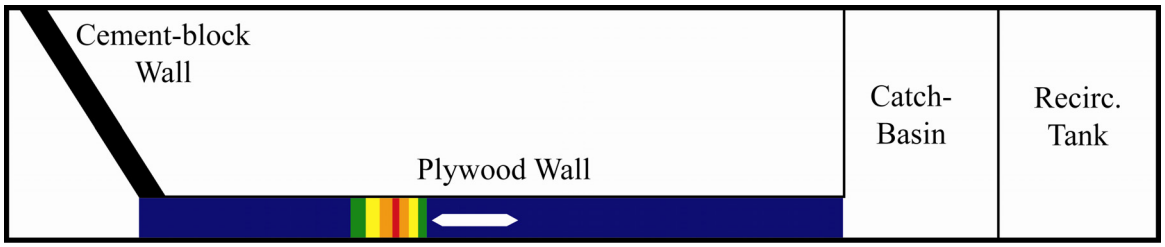

Figure 6-1: Plan view of flume setup. The colors in the channel indicate sediment depth at the start of each run in the second group of experiments (blue is 0.125 m, and red, though varying slightly with each run, was approximately 0.6 m. The slip-face slope was at angle of repose in still water). The white oblong object in the channel is the hydrophone case. A wire-mesh baffle was placed between the catch-basin and the recirculation tank to inhibit the movement of gravel into the recirculation mechanism. In practice, however, very little gravel was moved into the catch-basin, as nearly all the transport occurred on the top of the raised flat bed, or on the slip-slope of the synthetic dune. Note that the drawing is not to scale.

The channel was filled to a depth of approximately ⅛ m with #2 river stone, which had a size distribution shown in Figure 6-2. Two different types of experiments were performed. In the first, the sediment was piled in a 7.5-centimeter high, 0.6-meter long flat-bed immediately beneath, and centered longitudinally on, the hydrophone. This localized sediment motion to the region immediately adjacent to the hydrophone by increasing the shear stress on the raised bed. Decreasing the distance between source and hydrophone also increased the signal-to-noise ratio observed. It also enabled video monitoring of the total sediment transport occurring in the flume during the run.

In the second set of experiments, a large (approximately 0.6-meter high) gravel dune was built immediately upstream of the hydrophone. (See Figure 6-1.) The downstream face of the dune was established at the angle of repose for the sediment in still water. The purpose of this was to exploit the increased potential for sediment transport on the slip face of the dune to increase the range of transient transport rates that

could be observed with the flow rates that could be produced in the flume. The previously discussed benefits to localization of sediment motion near the hydrophone apply to this setup as well.

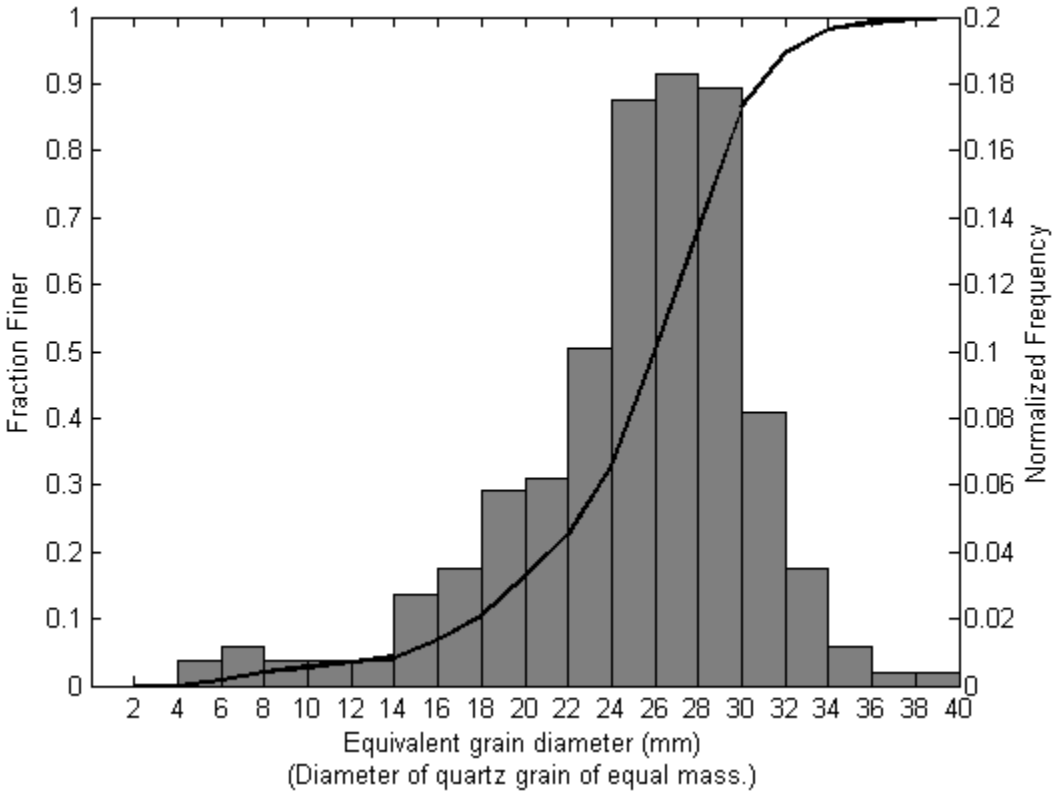

Figure 6-2: Size distribution of gravel used in the flume experiments, based on a random sample of 257 grains. $D_{50} \approx 26.0$ mm. Using a piecewise hermite spline interpolant to the cumulative distribution, $D_{15} \approx 19.6$ mm and $D_{85} \approx 29.8$ mm.

During each run, once the recording devices were running, the discharge in the flume was rapidly increased to a predetermined rate, and if the transport rate was seen to subside, then the discharge was usually increased. Because these experiments were not designed to test relations between discharge and transport rate, the only consideration was that there be a wide range of transport rates over the runs performed. In addition,

because both measurement techniques allow the resolution of rapid changes in the variables, it was not considered important (or desirable) that the transport rate be temporally stable.

Within each run, no attempt at a precise measure of water velocity or discharge was attempted. Discharge can be approximated using an empirical function of the pump speed (f, in Hz) based on data collected by the Penn State Civil Engineering Department and shown in Eq. 6.1, a relationship which is well behaved as long as the pump speed is kept below 30 Hz, which was true for all of the experiments reported here.

$$Q \approx e^{0.060\,f-3.6} \qquad \text{Eq. 6.1}$$

The parameters of the five runs are shown in Table 6-1. In the flat-bed runs, the pump speed was raised rapidly from a nontransport condition to the first speed listed, and if the transport rate decayed noticeably at that speed, then the discharge was increased. In the dune runs, the same general strategy was used, but in the third run, the transport rate was so high at the higher speed that sediment was regularly observed to collide with the hydrophone case. At this point, the discharge was decreased to an intermediate value. Collisions with the case were easy to identify on the acoustic record as well as the video, as the acoustic power generated in such a collision was typically two orders of magnitude greater than any other event recorded, and these data were discarded during analysis.

For all of the runs, the area of moving bed was limited to a 1.5 meter-long reach of the flume, and the leading and trailing edges of that region were watched carefully for movement outside of the region. During one run, extraregional movement was detected over a short interval (pump speed was reduced) and the corresponding data were omitted

from the analysis. Given that the channel width was 0.29 m, this provided a moving bed area of 0.435 m², which can be used to derive moving grain concentrations.

Table 6-1: Physical parameters of the flume runs

Sediment Configuration	**Pump Frequency (Hz)**	**Approximate Discharges (m^3/s) (see Eq. 6.1)**
Flat-bed	13 – 19	0.060 – 0.085
Flat-bed	24	0.12
Dune	13 – 15	0.060 – 0.067
Dune	13 – 15	0.060 – 0.067
Dune	13 – 15	0.060 – 0.067

Data Acquisition and Analysis

Video

A video camera was positioned to look down onto the bed at an approximate angle of 30° from the horizontal at the longitudinal location of the test reach described above. Floodlights positioned above the flume inside the glass illuminated the bed for the camera. Digital video tape recordings at 29.97 frames-per-second were converted to Audio-Video Interleave (AVI) files for computer processing and storage.

Synchronization of the audio (hydrophone) and video data was ensured by tapping on the side of the flume with a metal object well within the video frame. This produced a clearly audible signal on the hydrophone, and the moment of impact could be determined on the video to within the 0.04167 s that separate each frame. Three minutes of video were recorded from the time of the synchronization event for each run. The audio portion of the camera data was discarded.

The AVI files were processed using the VideoPoint motion analysis software package (Lenox Softworks). This package enables the user to extract position and velocities of moving objects as a function of time relative to established spatial axes and scales within the video. Two methods were used for processing the data. The majority of the data was processed by visually counting the number of moving grains (per unit area). This number is proportional to W', the weight per unit area included in the Bagnold bedload equation. The other term in that equation is U_b, the mean downstream velocity of the moving grains. This is much more difficult to measure, requiring the manual tracking of each sediment grain from frame to frame, and was computed only for a small subset of the data.

It became apparent, as soon as an attempt was made to overlay acoustic and video data, that either the camera or the AVI conversion process dropped frames. This caused a progressive shift in the video data throughout the three-minute clip. Because a second synchronization event was not performed (a simple fix for this problem), an internal synchronizing event had to be chosen. During some runs, a gravel grain impacted the hydrophone case and caused a noise several orders of magnitude louder than any other sound recorded. In one case, two grains collided with the case within a half-second of each other, which made the identification easier. A single event was chosen for each run, to avoid rubber-sheet effects, and a linear time correction was calculated as the ratio of the number of frames separating the synchronizing events in the video to the number of seconds separating the synchronizing events in the audio. This correction was then applied to the time stamp for each frame as shown in Eq. 6.2, where t' is the corrected

time, t is the original time, f_s is the nominal video sampling frequency in frames per second (29.97), and c_d is the observed sampling frequency in frames per second.

$$t' = t\left(1 + \frac{c_d}{f_s}\right) \qquad \text{Eq. 6.2}$$

This correction assumes that the frames were dropped at a constant rate throughout the recording process.

Hydrophone

The hydrophone case was rigidly mounted to the plywood wall of the channel, using a ½-inch threaded steel rod. The main amplifier was set to 100X gain through a single resistor, as the rotary switch modification described in Chapter 4 had not yet been made. Three minutes of hydrophone data were recorded for each run. Typically, transport began after twenty or thirty seconds, as the discharge in the flume was increased, which allowed about two-and-a-half minutes of useful data for each run.

Substantial noise was measured in the flume that was easily traceable to the hydraulic pump for the recirculation system. Mechanical vibration of the flume was also a likely source of noise. Noticeable resonance frequencies were noted in the spectra of the recordings. However, most of this noise was higher frequency than 1600 Hz, or lower than 125 Hz. (There were noticeable 60 and 120 Hz AC peaks, as well as fundamentals and overtones of the pump frequency. See Table 6-1 for frequencies.) Because of this, the acoustic power was summed over the range of 125 to 1600 Hz for this experiment,

although theoretical predictions by Thorne indicate that the peak frequencies for gravel should be near 10 kHz.

Correlation of hydrophone and video data was achieved by calculating the total power (between 125 and 1600 Hz; see above) in overlapping one-second time slices, centered on the time stamp. The acoustic signal was then interpolated, using a nearest neighbor scheme, to the frames of the video.

Results and Discussion

Flat-bed Experiment

Two runs were performed using the flat-bed approach. In the first run, the pump speed was about half as fast as that of the second. In the first run, the discharge was estimated at 0.084 m^3/s, while in the second, discharge was slowly increased to approximately 0.11 m^3/s.

Unit weight transport rates can be calculated using a form of Bagnold's bedload transport equation (Eq. 6.3), where i_b is the unit weight transport rate (in $Ns^{-1}m^{-1}$, or kg/s^3), U_b is the mean downstream velocity of the moving sediment, and W' is the weight of moving sediment per unit bed area.

$$i_b = W'U_b \qquad \text{Eq. 6.3}$$

To use this formulation, the assumption of equal mobility is necessary. (Because of the tight size distribution, this is probably reasonably accurate.) This assumption allows the use of a mean grain weight ($\overline{w}$ = 0.243 Newtons), calculated from the

sediment size distribution to convert the number of moving grains to a weight of moving grains. In terms of the variables that were measured, and given the bed area (A = 0.435 m²), over which motion was observed, the Bagnold relation becomes Eq. 6.4, where n is the number of moving grains.

$$i_b = U_b \frac{\overline{w} n}{A} \approx 0.559 n U_b \qquad \text{Eq. 6.4}$$

The lower transport rates of the first run allowed the individual grains to be tracked from frame-to-frame, which allows the calculation of grain velocities. In Figure 6-3, the results of the comparison between the number of moving grains and the total acoustic power are shown.

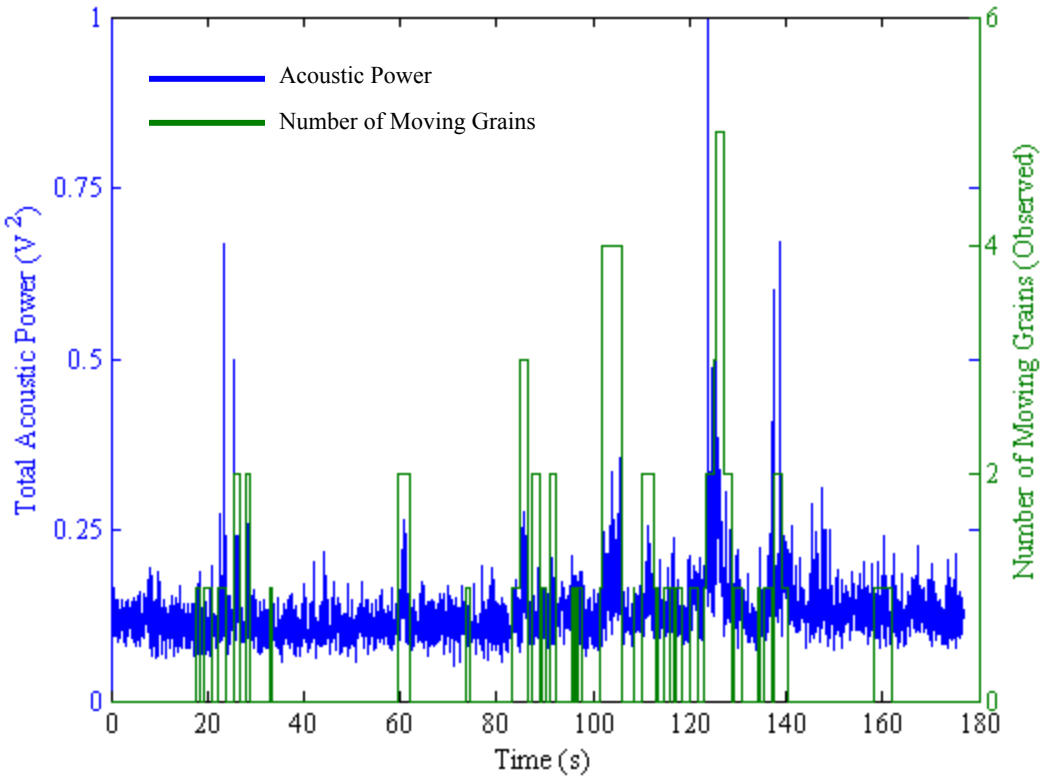

Figure 6-3: Total acoustic power ($125 \leq f \leq 1600$ Hz) for the first run of the flat-bed experiments, plotted with the number of moving grains from the digital video frames.

In Figure 6-4, the mean velocities are included to compare unit weight transport rates with the total acoustic power. It can be seen that acoustic power tracks reasonably well with both of these variables.

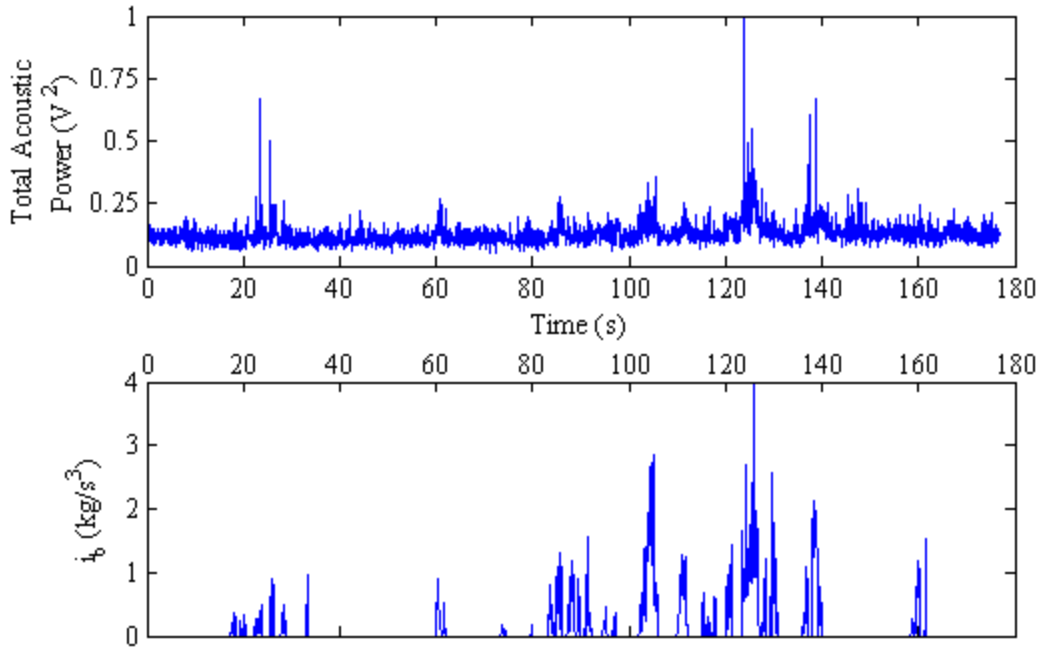

Figure 6-4: Total acoustic power ($125 \leq f \leq 1600$ Hz) for the first of the flat-bed experiments, plotted with Bagnold's unit weight transport rate, i_b, calculated as in the text.

The second run in this experiment had substantially higher discharge, and consequently much higher transport rates. Because of high sediment concentrations, and because particle velocities were higher, it was often difficult to track grains from one frame into another. To surmount this problem, a different processing technique was adopted. Using experience gained during the processing of the first run, the number of moving grains was estimated by eye for each frame of the second run.

Figure 6-5 shows the total acoustic power and the number of moving grains for the second run. This figure is analogous to Figure 6-3, and the difference in the transport rate between the two runs is clear in the range of the number of moving grains. It is also worth noting that the range of the total acoustic power has changed by two orders of magnitude.

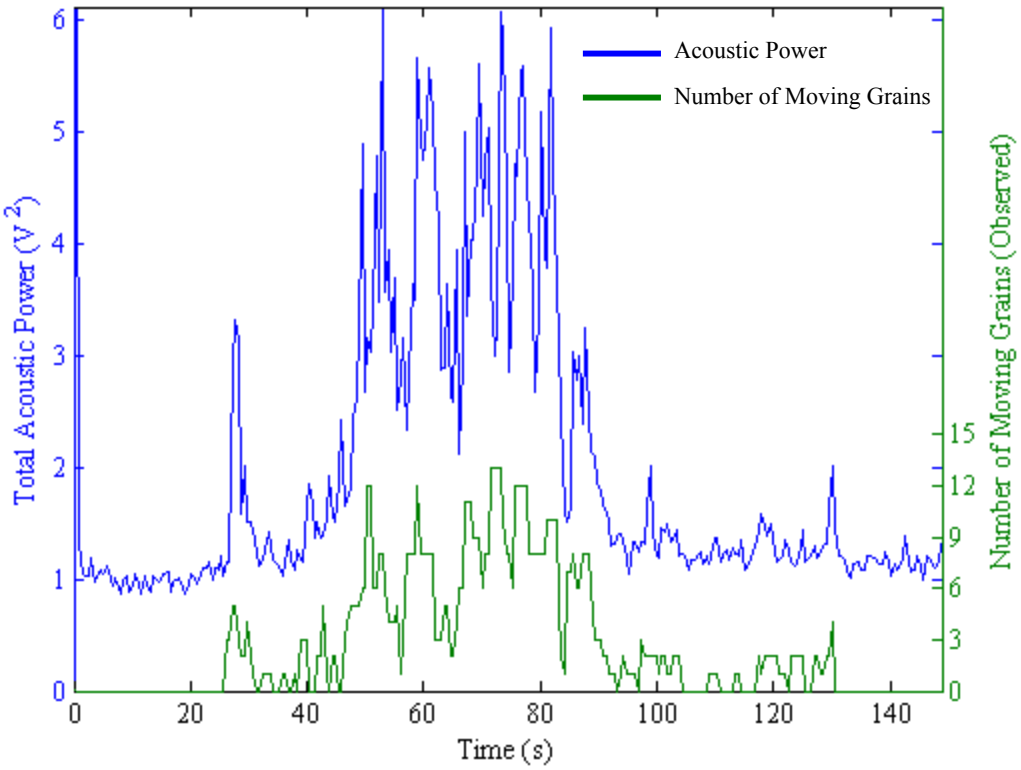

Figure 6-5: Total acoustic power ($125 \leq f \leq 1600$ Hz) for the second run of the flat-bed experiments. Note that the numbers of moving grains are approximately two to three times the numbers experienced in the first run (see Figure 6-3).

The missing variable in the analysis, the velocity of the grains, is expected to be well correlated with the number of moving grains, as both variables depend on the shear

stress near the bed. Using theoretical derivations for W' and U_b (Eq. 6.5 and Eq. 6.6) by Bridge and Dominic [1984], where a and α are constants:

$$U_b = a\left(U_* - U_{*c}\right) \qquad \text{Eq. 6.5}$$

$$W' = \left(\tau_0 - \tau_c\right)\tan\alpha \qquad \text{Eq. 6.6}$$

and by recalling the relationship between τ_0 and U_* (Eq. 6.7):

$$U_* \equiv \sqrt{\tau_0 / \rho} \qquad \text{Eq. 6.7}$$

Combining Eq. 6.3, Eq. 6.5, Eq. 6.6, and Eq. 6.7, we find Eq. 6.8.

$$i_b \propto \left(W'\right)^{3/2} \qquad \text{Eq. 6.8}$$

Figure 6-6 shows the total acoustic power as a function of the three-halves power of number of moving grains for the two runs in the flat-bed experiments. It is important to note that the standard error of the mean increases with the number of moving grains, mostly because the number of samples with high transport rates is very low. Because of this, it is unclear whether the relationship levels off at high transport rates or if this is an effect of the small sample size. In addition, all of the high-transport-rate samples come from the second run, when the number of moving grains was estimated by eye, and because this estimation becomes more difficult with higher sediment concentrations, the uncertainty is expected to be much higher.

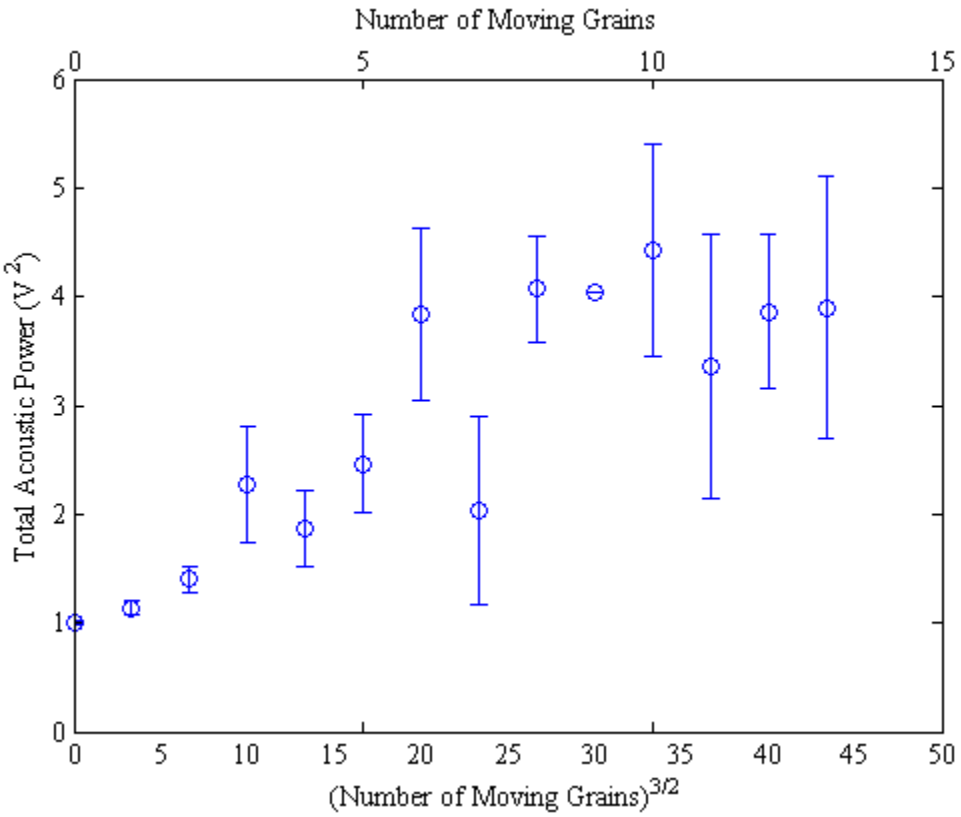

Figure 6-6: Relation between mean total acoustic power ($125 \leq f \leq 1600$ Hz) and the number of moving grains in both of the two runs in the flat-bed experiments. Spearman's correlation coefficient is 0.884. Vertical bars indicate two standard errors of the mean (circle).

Spearman's correlation coefficient is 0.884, which indicates that the model is a reasonably good fit. However, the data suggest that the constant of proportionality may change above about seven or eight moving grains.

Dune Experiments

In the second set of experiments, an attempt was made to gather data from higher transport rates by piling gravel into a dune, approximately 0.6 m high, placed so that the

slip face of the dune terminated at the upstream end of the hydrophone case. The results from one of these runs are shown in Figure 6-7.

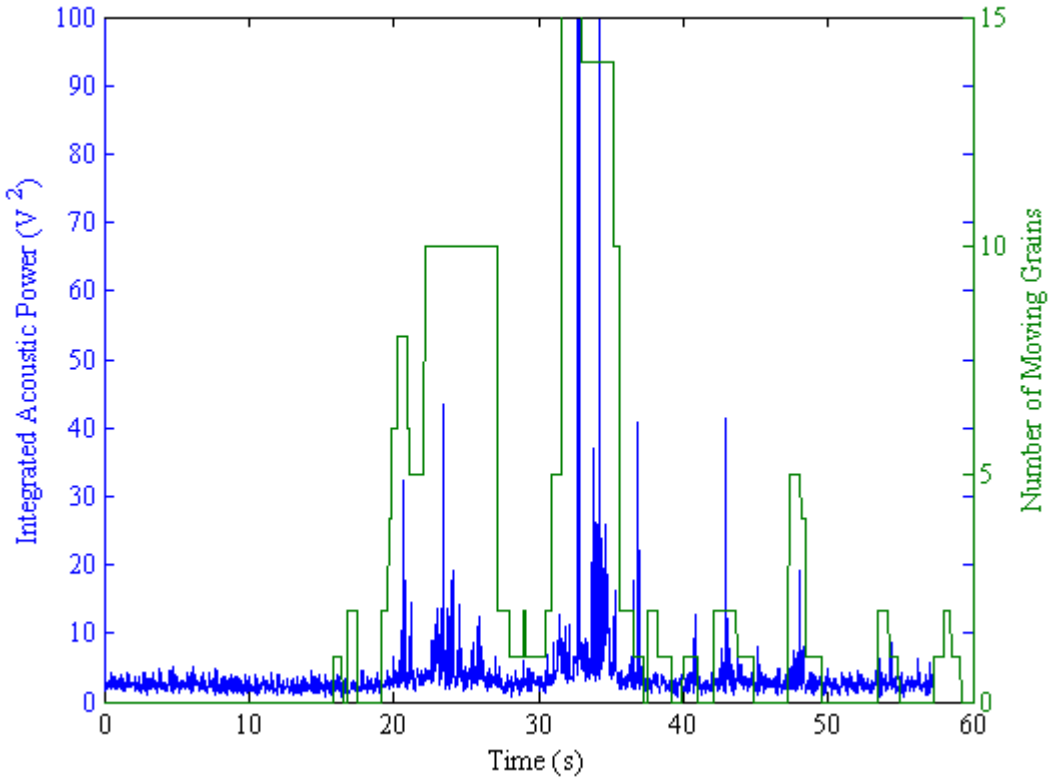

Figure 6-7: Sample results (from the second run) of the dune experiments. Note that the transient spike at about 33 seconds, shown clipped in this plot, is actually a double spike, and is the result of two gravel grains impacting on the hydrophone case.

Combining the results from three dune runs, Figure 6-8 shows the relationship between the acoustic power and the three-halves power of number of moving grains. The inset shows a parameter space comparable to that of Figure 6-6, and it is interesting that the linearity of the relationship is more evident, though the slope is lower. The standard errors of the means are smaller as there were many more frames when grains were in

motion than in the flat-bed experiments. The higher transport rates shown were achieved rarely, even with the dune formations, and so greater errors are associated with the means presented. Additional error is expected because of the difficulty of estimating the number of moving grains with these high concentrations. One possible explanation for the increased noise, relative to the linear increase seen in the lower transport rates, is that high concentrations of grains show increasing frequency of interparticle collision, which shortens the mean free path, and therefore increases the collision rate for a given number of moving grains.

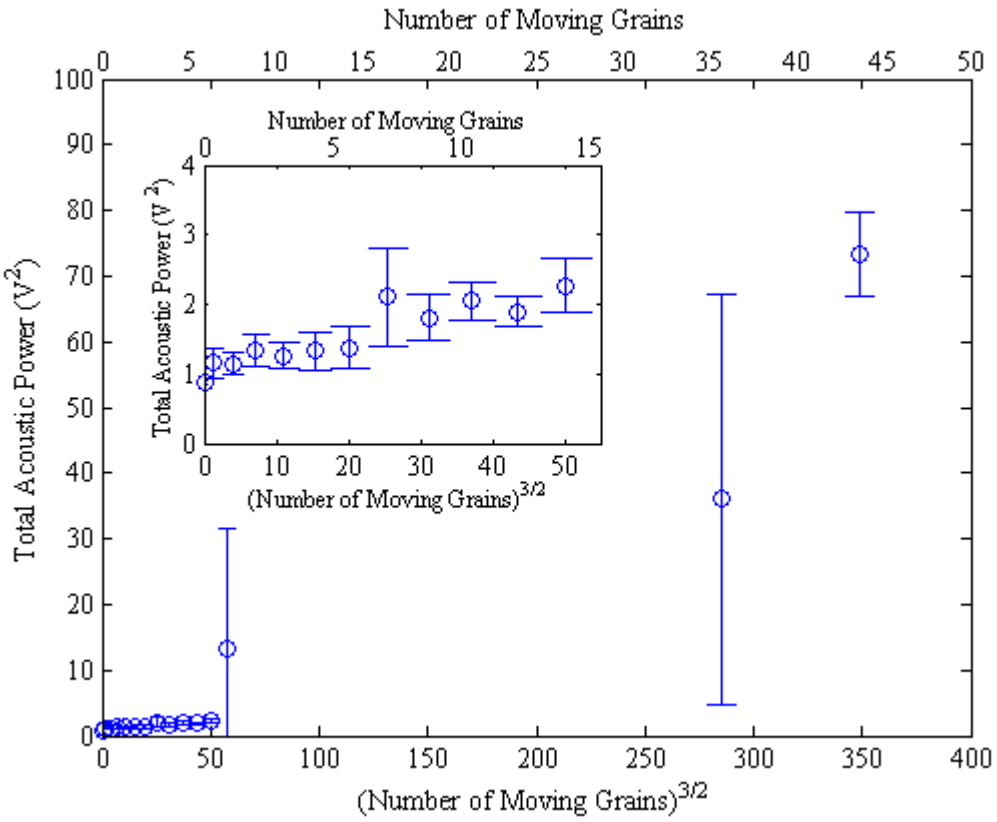

Figure 6-8: Relation between total acoustic power ($125 \leq f \leq 1600$ Hz) and the number of moving grains in the three dune runs. Vertical bars indicate two standard errors of the mean (circles). The inset shows a detailed plot of the results from a corresponding range of moving grains as that found in the flat-bed experiments.

Conclusions

It is clear from the data collected here that acoustic power in the range of 125 Hz to 1600 Hz is strongly correlated with the three-halves power of the number of moving grains in the bed, and therefore with the bedload transport rate, over the range of moving bed concentrations of 0 – 32 grains/m² (0 – 52 grains$^{3/2}$ moving over the 0.435 m² bed). Results from both the flat-bed and dune experiments support the linearity of the relationship between acoustic power and transport rate over these low concentrations. The dune study also examined higher transport rates over short intervals, and the data indicate that the relationship may not be linear at higher bedload concentrations. One possible explanation for this may be the shortening of the mean free path length, and consequent increased collision rate (and acoustic output) for a given number of moving grains.

The results of the flat-bed runs, showing that there is a clear and linear relationship between gravel transport and acoustic power at low transport rates, with the sensitivity falling off at higher transport rates, agree well with the results of previous flume studies [*Johnson and Muir*, 1969]. A possible theoretical explanation for this phenomenon was given by Jonys [1976]. However, the dune runs, which experienced much higher transport rates, and consequent high transport velocities, show an opposite effect, with acoustic power increasing compared to a linear fit. Speculatively, this increase may be due to a shortening of the mean free path length.

Because of the frequency sensitivity of the hydrophone used for these experiments, it was not possible to measure the full range of frequencies that were predicted in Chapter 3. This likely resulted in a loss in sensitivity of the system to changes in bedload transport rate.

Chapter 7

Field Study: Trinity River, California
May 2005

Modeling and flume results were sufficiently encouraging that the system needed to be tested in the field, where transport rates vary over a flood cycle. Also important is the comparison of the acoustic method to traditional pressure-difference sampling techniques. Although opinions on the accuracy of pressure-difference sampling vary widely throughout the scientific and engineering communities, it is undeniable that the large amount of historical data that exists requires that any new measurement technique be correlated with these methods.

Site Description and Dam Release

The Trinity River drains the western, southern, and eastern flanks of the Trinity Alps in Northern California (Figure 7-1). In 1964, a two-level dam system was completed. The upper dam, Trinity Dam, provides hydroelectric power to the region, while, about a kilometer downstream, Lewiston Dam diverts 75%-90% of the annual flow across the Coast Range divide, into the Sacramento Valley through the Clear Creek Tunnel into Whiskeytown Lake. In the late 1990s, the Trinity River Restoration Program was formed with the broad goal of increasing salmon and steelhead populations in the river. The plan instituted by the Program included a simulated snowmelt flood event in late April through July, with peak flows occurring in mid- to late-May. The maximum

flow was to be determined by the hydrologic budget for the water year. In 2005, a normal water year, dam discharge reached approximately 200 m^3/s.

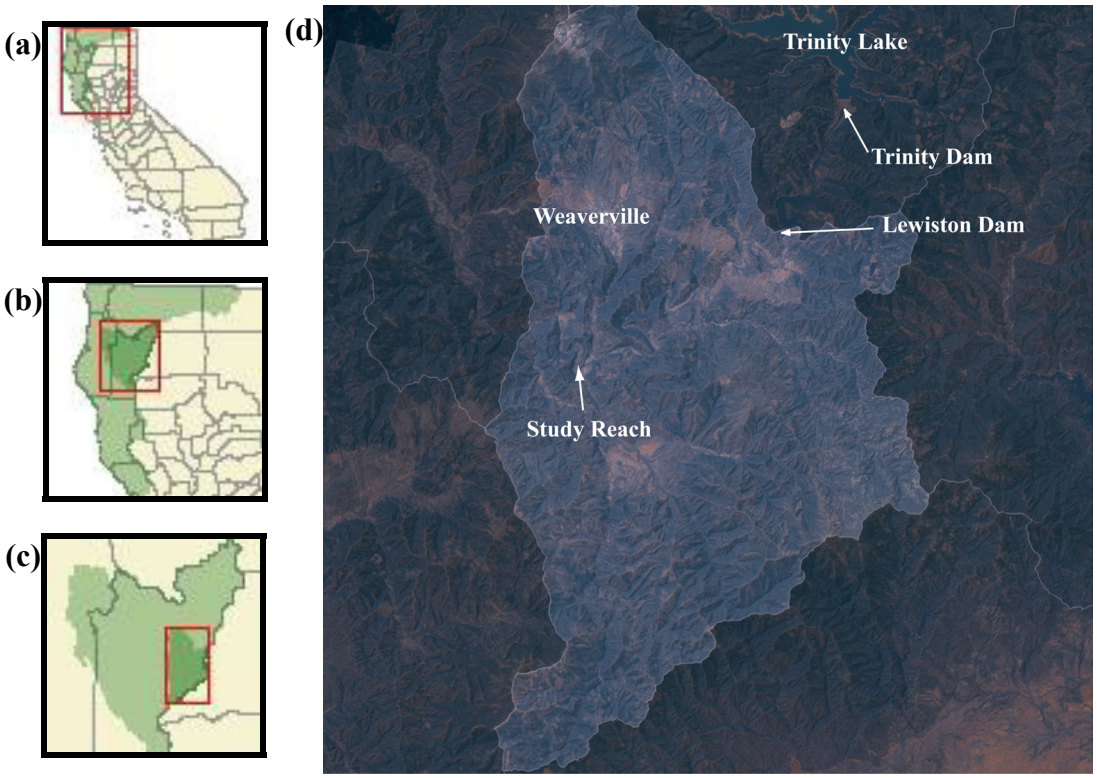

Figure 7-1: Location maps of the study site: **(a)** Northern California within California, **(b)** The Trinity basin within Northern California, and **(c)** the Middle Trinity basin within the Trinity River basin. **(d)** shows a satellite image of the Middle Trinity River basin (undimmed region). The Trinity River drains Trinity Lake (formerly Claire Engle Lake) through Trinity and Lewiston dams, and continues southwest towards the study reach, at Douglas City. Images from The California Spatial Library.

The acoustic method was tested at the Douglas City sediment monitoring site, which lies about 250 m downstream of the U.S. Geological Survey stream gauge (#11525854: Trinity River at Douglas City, CA, see Figure 7-2) from 6–19 May 2005. Figure 7-3 shows the dam discharge, and the provisional 15-minute discharge from the U.S. Geological Survey gauge at Douglas City, for the period 1–31 May 2006. The differences between the two represent both a 3-hour time lag between the dam and

Douglas City, and the influence of the tributaries that flow into the main stem between Lewiston and Douglas City. This influence is primarily noticeable on 8 and 17 May, when rain events caused high water in all of the major tributaries. In order to test the acoustic method, hydrophone recordings, taken from the right bank, were coordinated with traditional, pressure-difference bedload sampling by Graham Matthews and Associates (GMA), from a tethered cataraft about 4 m upstream. Observations by GMA indicate that the closest moving coarse bed material was approximately 10-12 meters away from the hydrophone during the study.

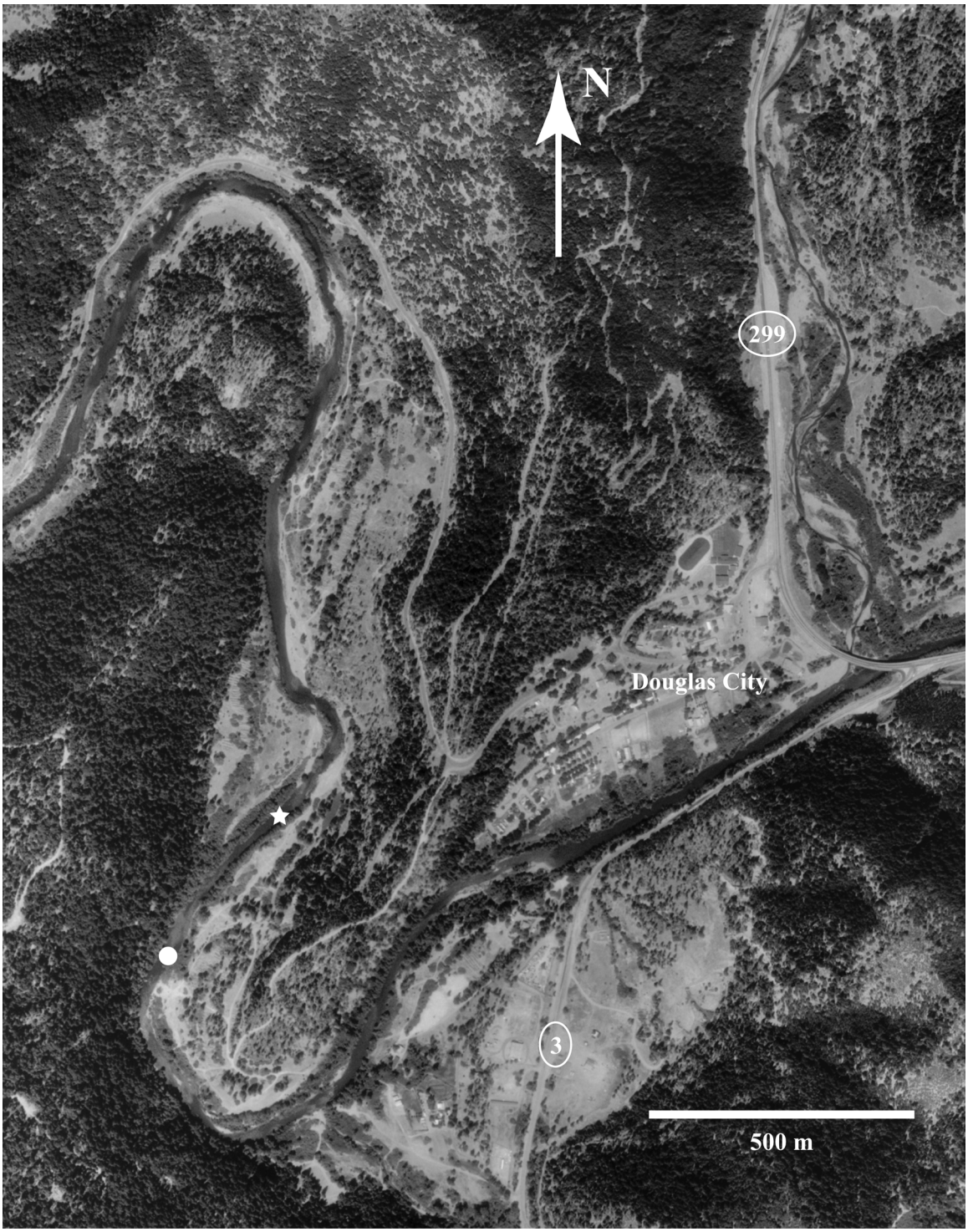

Figure 7-2: Aerial photograph showing study location. The pentagram shows the location of the pressure-difference sampling and hydrophone recordings. The circle shows the location of U.S.G.S. gauge #11525854, which was used for discharge comparison.

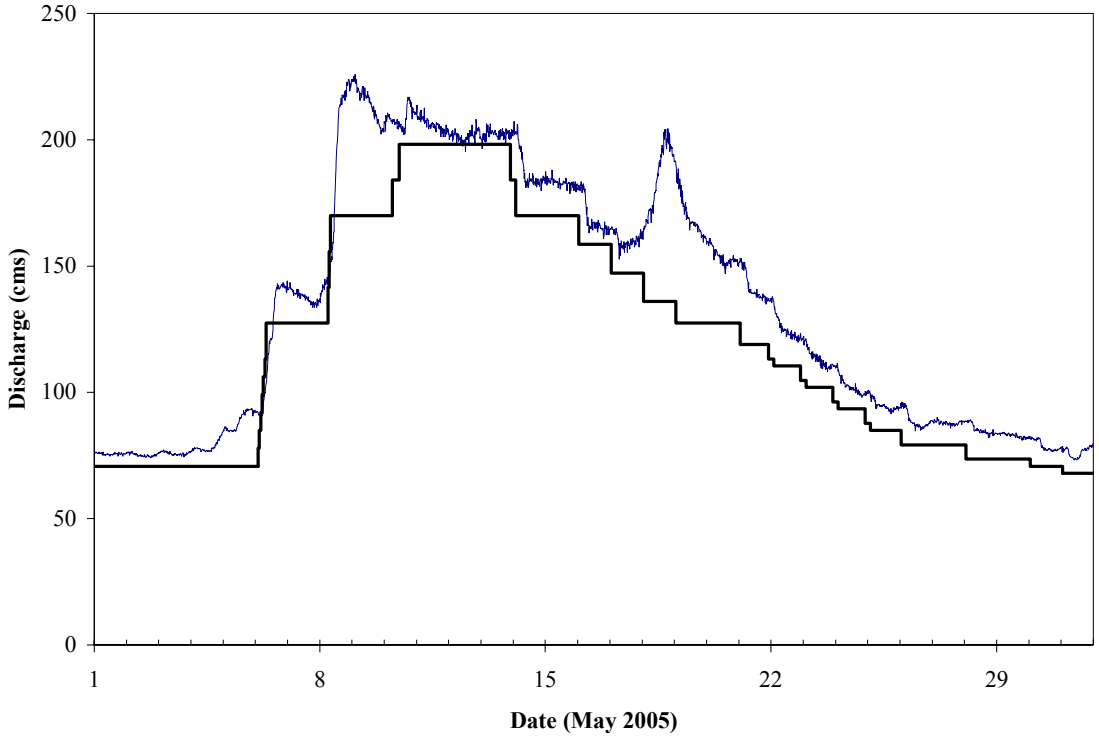

Figure 7-3: Plot of discharge from Lewiston Dam (black, stepped line), and gauge data from the U.S.G.S. gauge at Douglas City (blue line). There are several tributaries between Lewiston and Douglas City on the Trinity River (in particular: Rush Creek, Grass Valley Creek, Indian Creek and Weaver Creek), all of which contribute to the differences between the two discharges. Acoustic sampling was conducted only from 6 to 19 May.

Pressure-difference sampling

The following description of pressure difference sampling is based on a description supplied by Smokey Pittman, of GMA, and is included to give the reader necessary context for the comparison of the data generated by GMA and the acoustic data.

Bedload and suspended sediment transport data were collected at Douglas City during the Trinity flow release from 6 to 31 May 2005. Sampling was conducted from cataraft-based sampling platforms (20-foot inflatable tubes supporting a deck, crane and towers; see Figure 7-4) that were specifically developed for use on the Trinity River at sites where infrastructure for high flow sampling (bridge, cableway, etc.) was not in place.

Figure 7-4: Cataraft-based bedload sampling with the TR-2 sampler. Streamers show the location of the cable to which the cataraft is tethered. Photo by the author.

The catarafts were attached to temporary cable taglines (¼" galvanized wire rope) tensioned between large trees on either side of the channel. The cables were installed prior to the annual flow release at each site and removed after sampling. On the catarafts, the cable ran through a modified version of the U.S. Geological Survey standard boat equipment, which consisted of a pair of rollers on towers on either side of the platform.

The rollers were designed to allow quick release in the event of debris entanglement or other safety threats. The uprights kept the cable about six feet above the water surface, thereby allowing small boat traffic to pass by unobstructed during sampling activities. Caution signage and bright flagging were placed on cables to provide warning to other river users. During releases above 125 m^3/s, kayakers were stationed downstream of each cableway to assist personnel in the event of an emergency. Crews consisted of two on-river personnel specifically trained in cataraft-based sediment data collection, and sometimes a bank-observer responsible for data management. All crew members attended a mandatory safety/sampling technique training session on 5 May 2005. All crew leaders attended the U.S. Geological Survey Sediment Data Collection Techniques course in March 2005.

Bedload measurements were collected over a range of flows and at various positions on the hydrograph spanning the release period. Cataraft sampling involved use of a cable-deployed 6-inch Helley-Smith sampler with a 0.5-mm mesh collection bag, before 11 May, and a Toutle River-2 (TR-2) bedload sampler with a 0.5-mm mesh after that date. Cross sections were sampled at 12 to 20 verticals, following standard U.S. Geological Survey procedures [*Edwards and Glysson*, 1999] for Single Equal Width Increment samples. Typically, a sampler down-time of sixty seconds was used at each vertical. Because bedload transport at a station is often highly variable over short periods, two replicates (separate passes over the sampling cross section) were attempted for each sample. If only one pass could be completed due to time or safety considerations, the sample was flagged as such.

Samples (see Figure 7-5 for an example) were logged with site identifier, date, time, sampler-type, stage, moving bed width, sampler bottom time, and station information. Water temperature for each sample was obtained from in-channel temperature probes feeding data loggers. Water surface slopes were recorded for each distinct stage and all sites were photographed. Each sample replicate was dried and separated into half-phi-sizes down to one mm by sieving. Below 1 mm, only whole phi size classes were used. Subsequently, replicate data were combined into single-sample particle size distributions, reporting each size fraction as percent by weight of the total sample, and the partial mass sub-totals for fractions less than 0.5 mm, 0.5 to 8 mm and greater than 8 mm.

Figure 7-5: Photo of GMA TR-2 Sample 9 Pass 1 of 2, collected in the afternoon of 13 May. The black and white numbers on the portable rod indicate tenths of a foot (0.1 ft ≈ 3 cm).

Transport rates were computed for each size fraction using the standard methods of the U.S. Geological Survey as described in Edwards and Glysson [1999]. A station analysis for each sampling site was submitted along with the sample data and records to the U.S. Geological Survey for review/approval/publication in the U.S. Geological Survey California Science Center Annual Data Report Series. Suspended sediment samples were sent to the GMA Suspended Sediment Laboratory in Weaverville, and bedload samples were sent to the GMA Coarse Sediment Laboratory in Arcata. Quality assurance plans for both laboratories are available to interested parties through GMA.

Acoustic Data Collection

The hydrophone apparatus was rigidly anchored to the riverbed along the right bank, approximately ½ meter above the bed, and 4 meters downstream of the GMA cataraft tether cable. Safety considerations for the cataraft operators prohibited placing the hydrophone closer to the cableway. The system used in this study differed slightly from that presented in Chapter 4. In this case, the preamplifier was omitted from the system, as it malfunctioned during early field tests. The primary purpose of the preamplifier is to increase the signal volume relative to any noise that might be picked up over the long cable to the recording station. One of the dominant sources of noise, in such a system, is a 60-Hertz, alternating-current-induced magnetic field, which can be found close to power lines. This field site did not have power lines in the vicinity, and very little 60-Hertz noise was encountered, even without the preamplifier.

Acoustic data were recorded at intervals between 6 and 19 May. The system was not fully automated, and was not weatherproof, two limitations that dictated the duration and feasibility of data collection. Data were collected on ten of the fourteen days, usually for about eight hours, but some days were cut short because of rain. An effort was made, despite bad weather, to collect some data on each of the six days during which GMA made pressure-difference measurements.

Results and Discussion

Each one-minute file was divided into sixty one-second slices. Each slice was then transformed into the complex frequency domain using a 62500-point fast-Fourier transform. The power spectral density, derived from the fast-Fourier transform was then smoothed using a 10 Hz noncausal moving-median filter. The total acoustic power was estimated by performing a trapezoidal numerical integration of the smoothed power spectral density between 10 and 14809 Hz. The lower bound was selected to eliminate those bins dominated by leakage from the 0 Hz bin. The upper bound of 14809 Hz was selected because this is the frequency predicted theoretically by Thorne to correspond to the rigid-body radiation from the smallest gravel size (Krumbein φ = -3) [*Thorne*, 1986b]. The sixty one-second total power estimates were then averaged to give a mean total acoustic power for each one-minute sample.

Using an average value of all one-minute samples captured during each of the GMA sampling intervals (two passes, each approximately 45 minutes long), and assuming that the unit coarse bedload transport rate calculated by GMA corresponds to

an average rate over the interval during which the samples were collected, a least-squares linear regression between total acoustic power and the mass transport rate was computed (Figure 7-6).

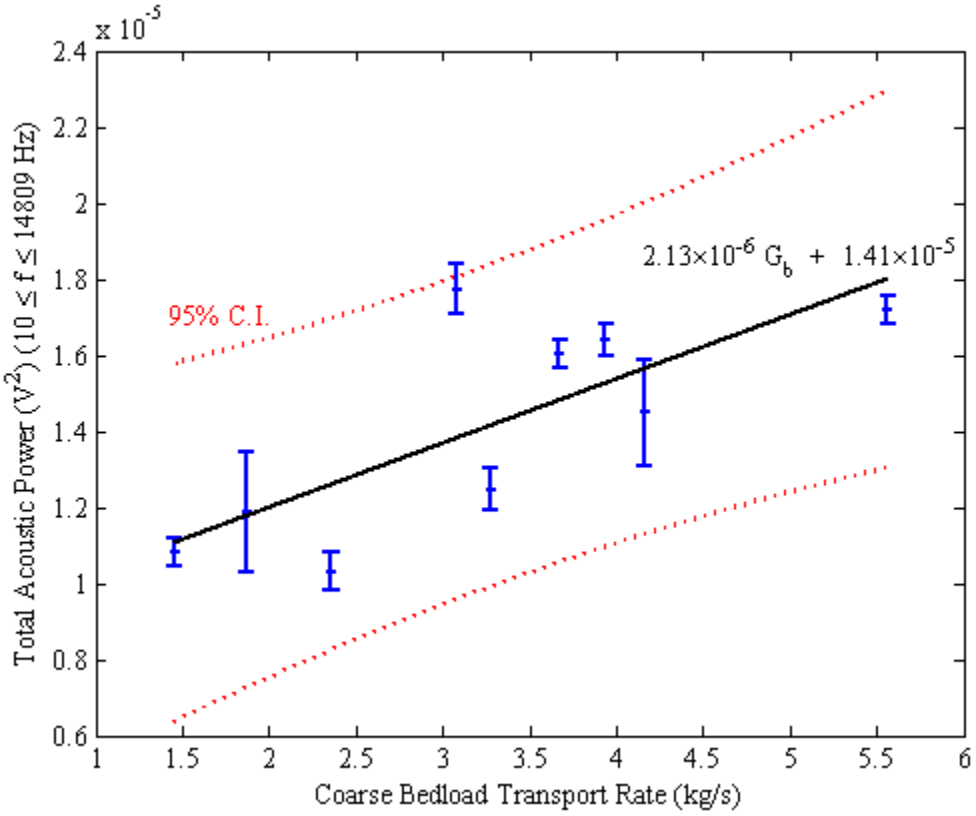

Figure 7-6: Correlation plot between temporally averaged total acoustic power and bedload transport rate for TR-2 measurements and acoustic samples. Error bars are ±2 standard errors of the mean. The Pearson's R is 0.758, with a p-value of 0.0180. Confidence interval for the parameters assumes Gaussian error. See text for details.

Seven GMA samples were excluded from this regression. Four were omitted because they were single-pass measurements made with the Helley-Smith sampler, and lack of data on the correlation between Helley-Smith and TR-2 measurements suggests that it might be incorrect to combine them in a single analysis. The other three samples that were rejected were collected on 20 May, and no acoustic data were collected during

those sample periods. A Pearson's correlation coefficient of 0.758 was observed between the variables; this coefficient has an exceedence probability of 1.80% for a population of this size.

This linear relationship between bedload transport rate and acoustic power was then used to predict bedload transport on the one-minute time scale for each of the 2400 acoustic sample points. The results are plotted, along with all sixteen GMA sample data, in Figure 7-7, which also shows the flood hydrograph at Douglas City. For the days when there are simultaneous measurements, the TR-2 measurements fall within the range of the predictions from the acoustic data, and those collected on 20 May match qualitatively with the acoustic data collected on 19 May. The acoustics technique consistently underpredicts the Helley-Smith measurements. It is unclear at this time whether the underprediction is caused by a difference in the sampling efficiencies of the Helley-Smith and TR-2 samplers, or by a difference in the acoustic environment of the early stages of the flood, though the former seems more likely.

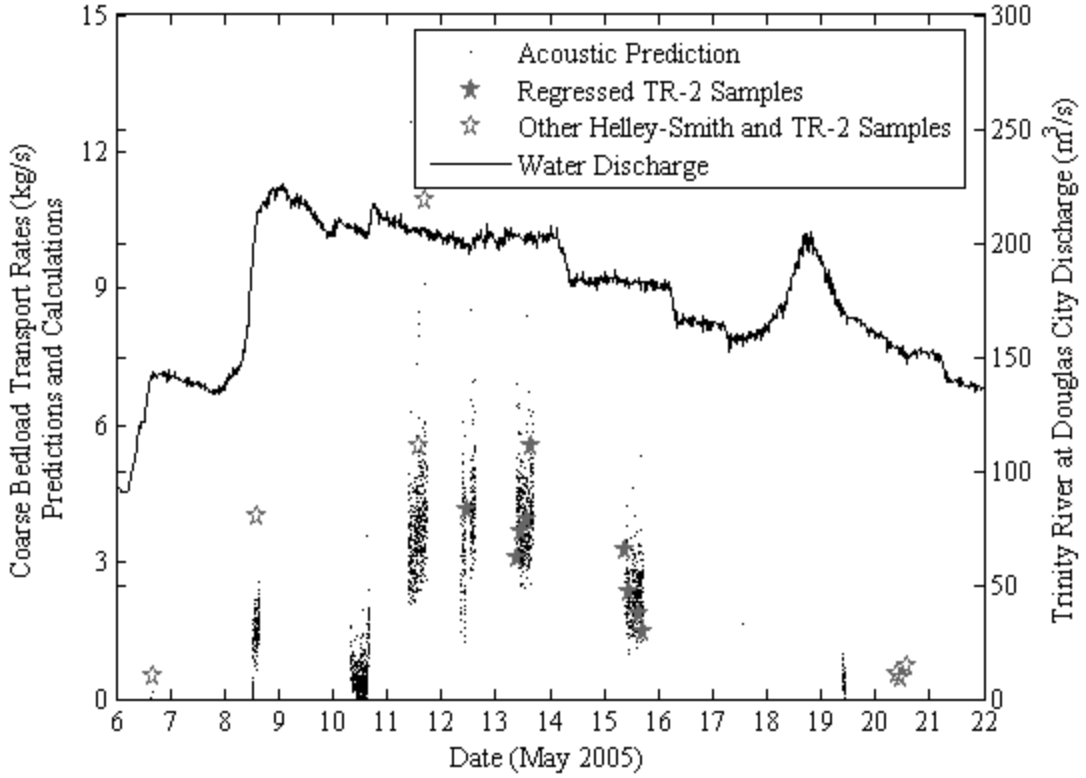

Figure 7-7: Acoustic bedload predictions (small black dots), compared with the GMA bedload transport rates. The hollow pentagrams were not used in the correlation analysis shown in Figure 7-6. Discharge at U.S. Geological Survey gauge #11525854 (see Figure 7-2 for location) is shown for comparison. Note that the GMA Helley-Smith samples (6–11 May) are single-pass samples, while the others are averages of two passes. Also, note that the 8 May observation is based on a partial sample because of dangerous river conditions.

Smoothing of the one-minute predictions, using a ten-minute moving-window median average (to reduce the importance of transient spikes), reveals distinct peaks and troughs in the power of the acoustic signal, and by inference, in the bedload transport (Figure 7-8). Interpretation of the spectral content of the one-minute predictions shows several interesting periodicities in the bedload transport rate. In particular, the lowest frequency peak that is captured by the spectral analysis, at a period of about 20 minutes,

is consistent with peak frequencies reported in the literature [*Whiting, et al.*, 1988] for periodic passage of bedload sheets. At shorter periods, there is a double peak at nine and six minutes, which may also be related to bedform movement. Higher frequency peaks may be related to periodicity in turbulent bursting phenomena known to play a significant role in bedload transport [*Heathershaw and Thorne*, 1985].

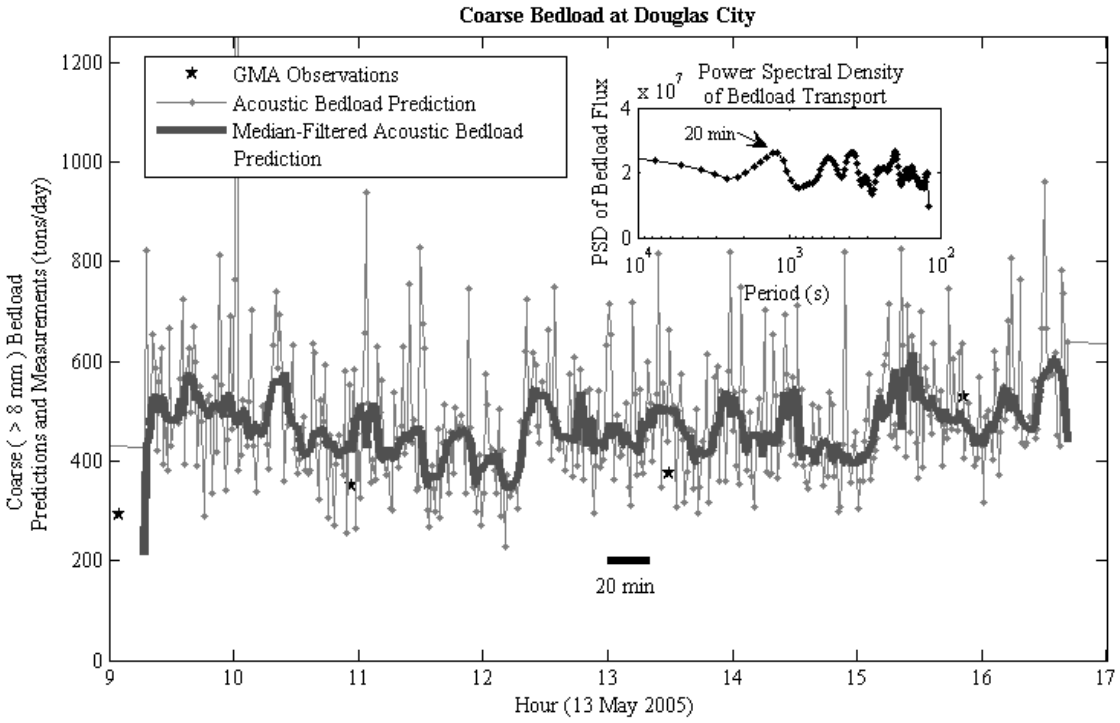

Figure 7-8: Detail of bedload transport predictions for 13 May 2005. The grey dots are the predicted values; the thin lines are interpolations. The thick curve is the result of a 10-minute moving window median filter. Inset is the power spectral density of the one-minute data. Note that the inset horizontal axis is logarithmically descending in period from 2¾ hours to 1⅔ minutes.

It has been suggested [e.g. *Clifford, et al.*, 1990] that acoustic noise will correlate strongly with discharge because of bubble collapse and turbulence-induced noise. Figure 7-9 shows the relationship between discharge and acoustic power. The dramatic rise in acoustic power well after the peak in water discharge cannot be attributed to

hydraulic noise, which we postulate would be the same for identical discharges on the rising and falling limbs of the hydrograph. We attribute this power rise to increased bedload transport during the falling stage, although the hysteresis pattern in this plot is reversed when compared to the traditional view of sediment transport in a flood. A review of the GMA data from Douglas City during the 2004 release shows a similar pattern in the days immediately surrounding the peak flow. This type of hysteresis loop (counterclockwise) is consistent with a system that experiences a delay in sediment supply to the study site [*Nistor and Church*, 2005]. We conjecture that the coarse sediment sources for this site are the deltas of Indian and Weaver Creeks located 2.5-3 miles upstream. Over the year, flooding driven by rainfall causes progradation of these deltas into the Trinity River. It is only during the dam-release flows that material is remobilized from the delta and transported downstream. We speculate that the peak of the coarse-material transport rate corresponds with the arrival of the deltaic material, and that this arrival lags behind the peak of the hydrograph. If this is indeed the case, then the distance and delay correspond to an average celerity of the sediment pulse of between 0.009 and 0.012 m/s, which is well within the range given in the literature for bedload sheet migration [e.g. *Whiting, et al.*, 1988].

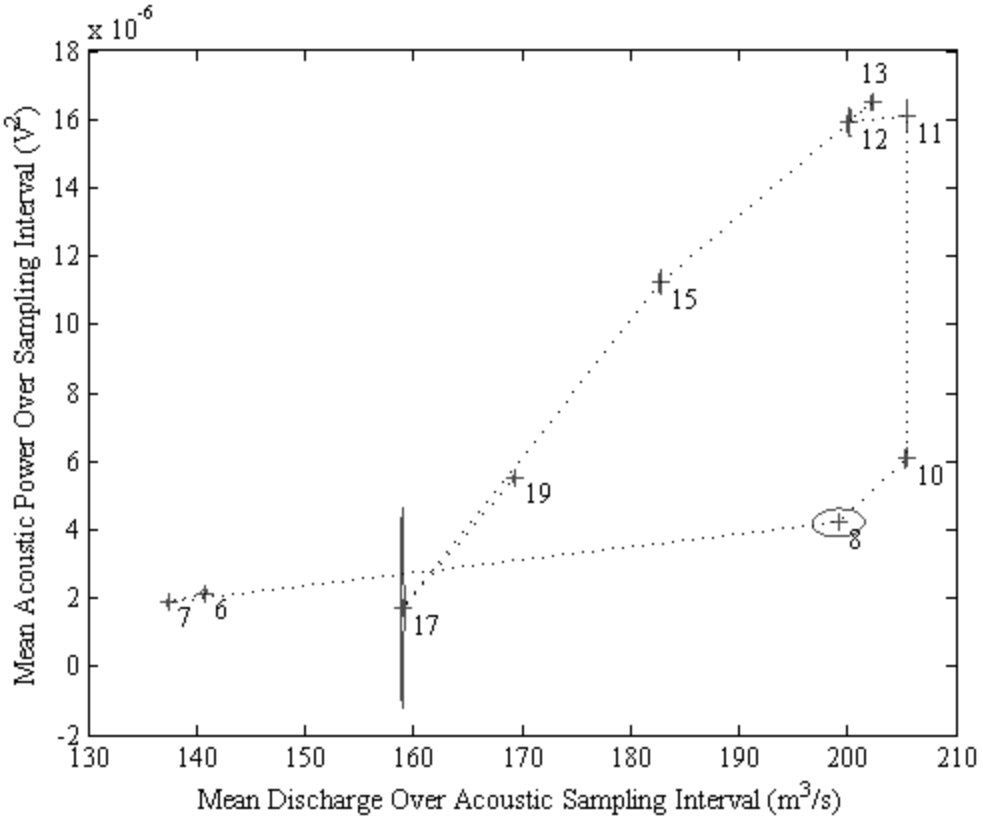

Figure 7-9: Relationship between mean acoustic power and mean discharge. Each daily value was calculated by averaging the acoustic samples collected on that day, and averaging linear interpolations of the 15-minute discharge data for each acoustic data point. The locations of the means are marked with a cross. The numbers indicate the date in May 2005. The ellipses indicate two standard errors of the means. Relatively few data points were collected on 17 May, because of rain, which may partly explain the large uncertainty in the data on that date. Note that in all cases except for 8 May and 17 May, the variability in discharge is so slight as to make the ellipse appear as a vertical bar.

Conclusions

Although the data are limited, a statistically significant correlation exists between acoustic power and bedload transport. The correlation cannot be attributed to a third variable dependent on discharge such as entrained-bubble collapse or turbulence, because the acoustic power during the rising limb was strongly separated from that during the

falling limb. The few data points of traditional data collected did not allow a test population for the relationship that was developed. Although no rigorous test is possible with the TR-2 data omitted from the regression (because no contemporaneous acoustic data was acquired) it is encouraging to note that proximate acoustic predictions are consistent with these observations.

Excluding a few, transient acoustic spikes, the observed range of the acoustic data appears to result from short-term trends rather than Gaussian scatter. Spectral analysis of the one-minute data shows several discrete frequency peaks; the lowest of these fall within the range of frequencies observed for bedload sheets.

Assuming that this model for the relationship between acoustic power and bedload transport rate is effective, observations about the bedload transport in the Trinity River at Douglas City during floods can be made. The hysteretic relationship observed is caused by delayed introduction of bedload material into the study reach. This delay can be explained by the travel-time necessary for bedload material to arrive at the reach from two tributary deltas where coarse material accumulates between dam releases.

Chapter 8

Conclusions and Future Directions

Conclusions

Total acoustic power, as measured by a relatively inexpensive hydrophone and amplified by a two-stage amplification system, is well-correlated with coarse bedload transport. The method will require extensive calibration for each site at which it is deployed.

In this study, the use of the Geospace MP-18 hydrophone limited the range of frequencies that were used to calculate the total acoustic power to those less than about 2000 Hz. In spite of this limitation, the correlation between total power and measured transport rate was good in both the flume and field setting.

A flume study showed that this acoustic method is capable of detecting very short-term (<1 second) fluctuations in the bedload transport when transport is localized near the hydrophone. In larger scale studies, the spatial integration intrinsic to the model will tend to smooth these high-frequency fluctuations, but reach-scale fluctuations should be similarly obvious. The flume study also suggests that at high sediment concentrations, the theoretical linearity between acoustic power and bedload transport rate may break down because of changes in the mean free path length.

A field study showed that the acoustic prediction tracks well over day-scale changes in bedload transport rate compared with pressure-difference sampling. The field

data also support that minute-scale trends in the bedload transport rate are observable when the received signal is spatially integrated, and some of the trends suggest the presence of bedload sheets moving through the reach. The presence of a hysteresis loop indicates that the variation observed in the acoustic signal cannot be due to variation in variables that are correlated with discharge.

Computer modeling supports the linear relationship between bedload transport and acoustic power that was observed in these studies and elsewhere. The linearity of the relationship seems to be robust even when sediment size distributions are changing. Also, modeling showed that the use of a limited range of frequencies, such as those used in this study, does not invalidate the linear relationship predicted between acoustic power and bedload transport rate.

The results from the flume and field studies clearly indicate that there is a strong correlation between bedload transport and acoustic power. Because of this, the null hypothesis that bedload transport cannot be inferred from the acoustic power can be rejected. The second null hypothesis, that the relationship between transport and acoustic power is nonlinear, cannot be rejected, because of the ambiguous flume data. However, results indicate that at low bedload concentrations, the deviation from linearity may be insignificant. The third null hypothesis, that measurements of acoustic power cannot be used as a proxy for bedload transport in a viable field instrument system is rejected based on the success of the system at the Trinity River site. More data from future dam releases will help to confirm this rejection.

Future Work

To more fully develop this method, several additional facets need to be addressed. Of primary importance is the collection of an additional field data set to complement the data presented in Chapter 6. This is underway, with the data collection performed by Graham Matthews and Associates, during the Trinity River 2006 release. The collection of these data will enable the comparison of the 2006 pressure-difference data with acoustic predictions based on the relations developed using the 2005 data. This will give an important insight into the durability of the observed correlation.

Modeling results indicate that a single instrument deployment is extremely sensitive to the spatial distribution of the bedload transport rate over the cross-section. This will have important ramifications concerning the applicability of calibration relations over channel-forming events. More investigations are needed into the potential usefulness of the deployment of multiple hydrophones, particularly into the instrumentation of both banks of a single cross-section, and into the sensitivity of the prediction to the placement of the single or multiple hydrophones. Configuration of a hydrophone array may yield important insight into the location of bedload transport in the cross-section, especially into changes in that location during the course of a flood. The placement of additional hydrophones (or arrays of hydrophones) in the streamwise direction could allow the observation, through correlation analysis, of waves of sediment (such as bedload sheets) passing the sensors.

Investigation is necessary into the use of a different hydrophone, with a wider frequency range, or perhaps multiple hydrophones with complementary frequency

ranges, to cover the range of frequencies from 0 to 20 kHz. Using these truly wideband frequency data, investigations can be made into the use of frequency content for the prediction of size distributions, following up on those made by Thorne [1986b].

Third, investigation is necessary into the use of a different hydrophone, with a wider frequency range, or perhaps multiple hydrophones with different frequency ranges, to cover a range of frequencies from 0 to 20 kHz. Using this truly wideband frequency data, investigations can be made into the use of the frequency content for the prediction of size distributions that has been reported by Thorne [1986b].

Bibliography

Akay, A., and T. H. Hodgson (1978), Acoustic radiation from the elastic impact of a sphere with a slab *Appl. Acoust.*, *11*, 285-304.

Akay, A., and T. H. Hodgson (1978b), Sound radiation from an accelerated or decelerated sphere, *J. Acoust. Soc. Am.*, *63*(2), 313-318.

Alcalde, A. M., G. E. Marques, G. Weber, and T. L. Reinecke (2000), Electron-acoustic-phonon scattering rates in II-VI quantum dots: contribution of the macroscopic deformation potential, *Solid State Communications*, *116*, 247-252.

Anderson, M. G. (1976), An inexpensive circuit design for the acoustic detection of oscillations in bedload transport in natural streams, *Earth Surface Processes*, *1*(3), 213-217.

Bänziger, R., and H. Burch (1990), Acoustic sensors (hydrophones) as indicators for bed load transport in a mountain torrent, paper presented at: Hydrology in Mountainous Regions I — Hydrological Measurements; The Water Cycle, International Association of Hydrological Sciences, Lausanne, August, 1990.

Barton, J. S., R. L. Slingerland, S. Pittman, and T. B. Gabrielson (submitted), Passive acoustic monitoring of coarse bedload transport on the Trinity River, California, *Water Resour. Res.*

Bedeus, K., and L. Ivicsics (1964), Observation of the noise of bed load, paper presented at: General Assembly, Commission on Hydrometry, International Association of Hydrological Sciences, Berkeley, CA, USA, 19-31 August 1963.

Bogen, J., and K. Møen (2001), Bed load measurements with a new passive ultrasonic sensor, paper presented at: Erosion and Sediment Transport Measurement: Technological and Methodological Advances, International Association of Hydrological Sciences, Oslo, NO, 19-21 June 2001.

Braudeau, G. (1951), Quelques techniques pour l'étude et la mesure du débit solid, *La Houille Blanche*, *6*(Special Issue A), 243-252.

Bridge, J. S., and D. F. Dominic (1984), Bed load grain velocities and sediment transport rates, *Water Resour. Res.*, *20*, 476-490.

Carling, P. A., I. Benson, and K. Richardson (2001), A new instrument to record sediment movement in bedrock channels, paper presented at: Erosion and Sediment Transport Measurement: Technological and Methodological Advances, International Association of Hydrological Sciences, Oslo, NO, 19-21 June 2001.

Childers, D. (1999), Field Comparisons of Six Pressure-Difference Bedload Samplers in High-Energy Flow, 59 p. pp., U.S. Department of the Interior, U.S. Geological Survey, Vancouver, WA, 1999.

Clifford, N. J., J. McClatchey, and J. R. French (1990), Measurements of turbulence in the benthic boundary layer over a gravel bed and Comparison between acoustic measurements and predictions of the bedload transport of marine gravels — Discussion, *Sedimentology*, *37*, 161-171.

Downing, J., P. J. Farley, K. Bunte, K. Swingle, S. E. Ryan, and M. Dixon (2001), Acoustic gravel-tranport sensor: description and field tests in Little Granite Creek, Wyoming, USA, paper presented at: Erosion and Sediment Transport Measurement: Technological and Methodological Advances, International Association of Hydrological Sciences, Oslo, NO, 19-21 June 2001.

Downing, J., and S. E. Ryan (2001), Field comparisons of the Elwha bedload sampler and an acoustic gravel-transport sensor: Middle Fork of the Piedra River, Colorado, USA, *EOS Trans. AGU, Fall Meet. Suppl.*, H21B-0299.

Einstein, H. A. (1944), Bed-load transportation in Mountain Creek, *Technical Bulletin 55*, 44 pp., U.S. Department of Agriculture Soil Conservation Service, Greenville, SC, USA, August 1944.

Emmett, W. W. (1980), A field calibration of the sediment-trapping characteristics of the Helley-Smith bedload sampler, *U.S. Geological Survey Professional Paper 1139*, 44 pp., U.S. Government Printing Office, Washington, DC, USA.

Froehlich, W. (2001), Monitoring of bed load transport by use of acoustic and magnetic device, paper presented at: Erosion and Sediment Transport Measurement: Technological and Methodological Advances, International Association of Hydrological Sciences, Oslo, 19-21 June.

Goldsmith, W. (2001), *Impact: The Theory and Physical Behaviour of Colliding Solids*, Dover ed., 379 pp., Dover Publications, Inc., Mineola, NY, US.

Govi, M., F. Maraga, and F. Moia (1993), Seismic detectors for continuous bed load monitoring in a gravel stream, *Hydrolog. Sci. J.*, *38*, 123-132.

Hartshorn, K., N. Hovius, W. B. Dade, and R. L. Slingerland (2002), Climate-driven bedrock incision in an active mountain belt, *Science*, *297*, 2036-2038.

Heathershaw, A. D., and P. D. Thorne (1985), Sea-bed noises reveal role of turbulent bursting phenomenon in sediment transport by tidal currents, *Nature*, *316*, 339-342.

Helley, E. J., and W. Smith (1971), Development and calibration of a pressure-difference bedload sampler, *Open File Report 73-108*, 18 pp., U.S. Department of the Interior, Geological Survey, Water Resources Division

Hinrich, H. (1970), Bedload measurement by means of bottom plates and bedload samplers with hydrophone attachments, paper presented at: Hydrometry Symposium, International Association of Hydrological Sciences, Koblenz, September.

Howard, A. D. (1998), Long profile development of bedrock channels: Interaction of weathering, mass wasting, bed erosion, and sediment transport, in *Rivers Over Rock: Fluvial Processes in Bedrock Channels*, *Geophysical Monograph Series*, vol. 107, edited by K. Tinkler and E. E. Wohl, pp. 297-318, American Geophysical Union, Washington, D.C.

Hubbell, D. W. (1964), Apparatus and Techniques for Measuring Bedload, *U.S. Geological Survey Water-Supply Paper 1748*, 74 pp., U.S. Government Printing Office, Washington, DC, USA.

Hubbell, D. W., H. H. Stevens, Jr., J. V. Skinner, and J. P. Beverage (1985), New approach to calibrating bedload samplers, *J. Hydraul. Eng.*, *111*(4), 677-694.

Johnson, P., and T. C. Muir (1969), Acoustic detection of sediment movement, *J. Hydraul. Res.*, *7*, 519-540.

Jonys, C. K. (1976), Acoustic measurement of sediment transport, *Canadian Inland Waters Directorate Scientific Series 66*, 118 pp., Inland Waters Directorate, Burlington, ON, CA.

Juniet, M. (1952), L'Arénaphone, un appareil détecteur des movements des sédiments fins, paper presented at: Transport Hydraulique et Décantation des Matériaux Solides, Deuxième Journées de L'Hydraulique, Société Hydrotechnique de France, Grenoble, FR.

Kinsler, L. E., and A. R. Frey (1962), *Fundamentals of Acoustics*, John Wiley & Sons, New York, NY.

Klingeman, P. C., R. T. Milhous, and T. L. Heinecke (1979), Oak Creek vortex bedload sampler, Water Resources Research Institute, Oregon State University, Corvallis.

Komar, P. D. (1987), Selective grain entrainment by a current from a bed of mixed sizes: A reanalysis, *Journal of Sedimentary Petrology*, *57*, 203-211.

Koss, L. L. (1974), Transient sound from colliding spheres — Normalized results, *J. Sound Vib.*, *36*(4), 541-553.

Koss, L. L., and R. J. Alfredson (1973), Transient sound radiated by spheres undergoing an elastic collision, *J. Sound Vib.*, *27*(1), 59-75.

Labaye, G. (1948), Note sur le débit solide des cours d'eau, *La Houille Blanche*, *3*(A).

Lewis, J. (1991), An improved bedload sampler, paper presented at: Fifth Federal Interagency Sedimentation Conference, Subcommittee on Sedimentation of the Interagency Advisory Committee on Water Data, Las Vegas, NV, 1-8 June 1991.

Love, A. E. H. (1944), *A Treatise On The Mathematical Theory of Elasticity*, 4th ed., 643 pp., Dover Publications, New York, NY, USA.

Millard, N. W. (1976), Noise generated by moving sediments, paper presented at: Conference on Recent Developments in Underwater Acoustics, Institute of Acoustics, London, UK, 31 March-1 April.

Mizuyama, T., M. Fujita, and M. Nonaka (2001), Measurement of bedload with the use of hydrophone in mountain torrents, paper presented at: Erosion and Sediment Transport Measurement: Technological and Methodological Advances, International Association of Hydrological Sciences, Oslo, NO, 19-21 June 2001.

Murray, D. (2002), Breathing mode vibrations of an isotropic elastic sphere surrounded by a fluid medium, University of British Columbia, Okanagan.

Nistor, C. J., and M. Church (2005), Suspended sediment transport regime in a debris-flow gully on Vancouver Island, British Columbia, *Hydrol. Process.*, *19*, 861-885, doi: 10.1002/hyp.5549.

Oppenheim, A. V., R. W. Schafer, and J. R. Buck (1999), *Discrete Time Signal Processing*, *Prentice Hall Signal Processing Series*, 2nd ed., 870 pp., Prentice Hall, Upper Saddle River, NJ, USA.

Ovsyuk, N. N., and V. N. Novikov (1996), Influence of a glass matrix on acoustic phonons confined in microcrystals, *Physical Review B*, *53*(6), 3113-3118.

Reid, I., J. T. Layman, and L. E. Frostick (1980), The continuous measurement of bedload discharge, *J. Hydraul. Res.*, *18*, 243-249.

Rennie, C. D., R. G. Millar, and M. A. Church (2002), Measurement of bed load velocity using an acoustic doppler current profiler, *J. Hydraul. Eng.*, *128*(5), 473-483.

Richards, K. S., and L. M. Milne (1979), Problems in the calibration of an acoustic device for the observation of bedload transport, *Earth Surface Processes*, *4*, 335-346.

Sklar, L. S., and W. E. Dietrich (1998), River longitudinal profiles and bedrock incision models: Stream power and the influence of sediment supply, in *Rivers Over Rock: Fluvial Processes in Bedrock Channels*, *Geophysical Monograph Series*, vol. 107, edited by K. Tinkler and E. E. Wohl, pp. 237-260, American Geophysical Union, Washington, D.C.

Sklar, L. S., and W. E. Dietrich (2004), A mechanistic model for river incision into bedrock by saltating bedload, *Water Resour. Res.*, *40*, W06301, doi: 10.1029/2003WR002496.

Slingerland, R. L., S. D. Willett, and H. L. Hennessey (1997), A new fluvial bedrock incision model based on the work-energy principle, *EOS Trans. AGU, Fall Meet. Suppl.*, *78*(46), F299.

Thorne, P. D. (1985), The measurement of acoustic noise generated by moving artificial sediments, *J. Acoust. Soc. Am.*, *78*, 1013-1023.

Thorne, P. D. (1986a), An intercomparison between visual and acoustic detection of gravel movement, *Mar. Geol.*, *72*, 11-31.

Thorne, P. D. (1986b), Laboratory and marine measurements on the acoustic detection of sediment transport, *J. Acoust. Soc. Am.*, *80*(3), 899-910.

Thorne, P. D. (1987), The acoustic measurement of gravel transport, paper presented at Fifth International Conference on Electronics for Ocean Technology, IERE, Edinburgh, UK, 24-26 March 1987.

Thorne, P. D. (1993), Seabed Saltation Noise, in *Natural Physical Sources of Underwater Sound*, edited by B. R. Kerman, pp. 721-744, Kluwer Academic, Dordrecht, NL.

Thorne, P. D., and D. J. Foden (1988), Generation of underwater sound by colliding spheres, *J. Acoust. Soc. Am.*, *84*(6), 2144-2152.

Thorne, P. D., A. D. Heathershaw, and L. Triano (1984), Acoustic detection of seabed gravel movement in turbulent tidal currents, *Mar. Geol.*, *54*, M43-M48.

Thorne, P. D., A. P. Salkield, and A. J. Marks (1983), Application of acoustic techniques in sediment transport research, paper presented at: Institute of Acoustics Conference on Acoustics and the Seabed, University of Bath, Bath, UK.

Thorne, P. D., J. J. Williams, and A. D. Heathershaw (1989), In situ acoustic measurements of marine gravel threshold and transport, *Sedimentology*, *36*, 61-74.

Tywoniuk, N., and R. G. Warnock (1973), Acoustic detection of bed-load transport, paper presented at: Hydrology Symposium, Department of Environment: Natural Resource Council, University of Alberta, Edmonton, Alberta, 8-9 May.

Voulgaris, G., M. P. Wilkin, and M. B. Collins (1994), Shingle movement under waves & currents: An instrumented platform for field data collection, in *Coastal Dynamics '94*, edited by A. S. Arcilla, et al., pp. 894-909, American Society of Civil Engineers.

Voulgaris, G., M. P. Wilkin, and M. B. Collins (1995), The in situ passive acoustic measurement of shingle movement under waves and currents: instrument (TOSCA) development and preliminary results, *Cont. Shelf Res.*, *15*(10), 1195-1211.

Whiting, P. J., W. E. Dietrich, L. B. Leopold, T. G. Drake, and R. L. Shreve (1988), Bedload sheets in heterogeneous sediment, *Geology*, *16*(2), 105-108.

Williams, J. J., P. D. Thorne, and A. D. Heathershaw (1989), Comparisons between acoustic measurements and predictions of the bedload transport of marine gravels, *Sedimentology*, *36*, 973-979.

VITA
Jonathan S. Barton

Education

The Pennsylvania State University, Ph.D. 2006.
Cornell University, Geological Sciences, B.A., 1997.

Experience

Teaching Assistant, Penn State University, Fall 2000–Spring 2002, Spring 2005.
Research Assistant, Penn State University, Summer 2000, Fall 2002–Fall 2004.
Scientific Programmer/Analyst, General Sciences Corporation (subsidiary of SAIC), NASA/Goddard Space Flight Center, Maryland, USA, July 1997–June 2000.

Selected Publications

Barton, J. S., R. L. Slingerland, S. Pittman, T. B. Gabrielson (submitted), Passive acoustic monitoring of coarse bedload transport on the Trinity River, California, *Water Resour. Res.*

Barton, J. S., R. L. Slingerland, S. Pittman, and T. B. Gabrielson (2006), Passive acoustic monitoring of coarse bedload transport on the Trinity River, paper presented at: 8th Federal Interagency Sedimentation Conf., Subcomm. on Sedimentation of the Advisory Comm. on Water Info., Reno, NV, US, 2-6 April 2006.

Barton, J. S., R. L. Slingerland, T. B. Gabrielson, and P. A. Johnson (2003), Listening to bedload: A flume study relating acoustic response to bedload motion, paper presented at: Federal Interagency Sediment Monitoring Instrument and Analysis Research Workshop, Subcommittee on Sedimentation of the Advisory Committee on Water Information, Flagstaff, AZ, US, 9-11 September 2003.

Barton, J. S., S. R. Miller, R. L. Slingerland, T. B. Gabrielson, and N. Hovius (2002), Passive acoustic sensing of fluvial bedload transport: a flume study, *EOS Trans. AGU, Fall Meet. Suppl.*, *83*(47), Abstract H21C-0813.

Barton, J. S., D. K. Hall, and G. A. Riggs (2000), Remote sensing of fractional snow cover using Moderate Resolution Imaging Spectroradiometer (MODIS) data, paper presented at: 57th Eastern Snow Conference, Syracuse, NY, US, 17-19 May.

Foster, J. L., J. S. Barton, A. T. C. Chang, and D. K. Hall (2000), Snow crystal orientation effects on the scattering of passive microwave radiation, *IEEE T. Geosci. Remote*, *38*(5), 2430-2434.

Hall, D. K., R. S. Williams, Jr., J. S. Barton, O. Sigurðsson, L. C. Smith, and J. B. Garvin (2000), Evaluation of Remote Sensing Techniques to Measure Decadal-Scale Changes in the Mass Balance of Hofsjökull Ice Cap, Iceland, *J. Glaciol.*, *46*(154), 375-388.

Barton, J. S., D. K. Hall, O. Sigurðsson, R. S. Williams, Jr., L. C. Smith, and J. B. Garvin (1999), Calculation and error analysis of a digital elevation model of Hofsjökull, Iceland from SAR interferometry, paper presented at: 56th Eastern Snow Conference, Fredericton, NB, CA, 2-4 June 1999.

Barton, J. S., D. K. Hall, O. Sigurðsson, R. S. Williams, Jr., L. C. Smith, and J. B. Garvin (1998), Digital elevation model calculation of Hofsjökull, Iceland, using ERS-1/-2 tandem SAR interferometry, *EOS Trans. AGU, Fall Meet. Suppl.*, *79*(45), Abstract H11B-20.